Available online at www.sciencedirect.com
SCIENCE DIRECT®
Icarus 174 (2005) 419–443
ICARUS
www.elsevier.com/locate/icarus

The effects of martian orbital variations upon the sublimation and relaxation of north polar troughs and scarps

Asmin V. Pathare [a,b,*], David A. Paige [b]

[a] *Division of Geological and Planetary Sciences, Caltech, Mail Stop 150-21, Pasadena, CA 91125, USA*
[b] *Department of Earth and Space Sciences, University of California, Los Angeles, CA 90095, USA*

Received 4 February 2004; revised 29 September 2004

Abstract

The North Polar Layered Deposits (PLD) of Mars are climatologically significant because they represent the largest actively-exchanging reservoir of martian water. The kilometer-scale topography of the North PLD is dominated by troughs and scarps, which exhibit highly-correlated surface slopes and total depths. The most widespread theories of PLD evolution presume that the asymmetrical nature of North PLD troughs (characterized by equatorward-facing slopes that are generally steeper than poleward-facing slopes) is the result of preferential H_2O sublimation from equatorward-facing trough walls. However, our orbitally-modulated simulations indicate that there is no long-term sublimation advantage of equatorward-facing trough walls, because of the effects of obliquity upon the slope dependence of sublimation rate. In contrast, we propose that viscous relaxation of subsurface water is consistent with the slope and depth distributions of North PLD troughs and scarps. The results of our finite element simulations suggest that a mere 2 K difference in the subsurface temperatures of opposing trough walls is sufficient to produce the observed slope disparity, due to the slower rate of uplift of colder poleward-facing trough walls. Both our sublimation and relaxation simulations indicate that present-day North PLD troughs have formed since 5 Ma and are not sites of long-term deposition; additionally, our results imply that glacial flow may govern the large-scale evolution of the North PLD, especially at high obliquity.

Keywords: Mars, surface; Ices; Mars, climate

Introduction

The North Polar Layered Deposits (PLD) represent the largest actively-exchanging reservoir of water on Mars. The characteristic rhythmic layering of the PLD (Fig. 1) strongly suggests that orbital variations have modulated their formation (Murray et al., 1972; Thomas et al., 1992). The obliquity of Mars varies far more dramatically than its terrestrial counterpart (Fig. 2), as over the last 10 Myr martian obliquity has departed considerably from its current Earth-like value of 25.2°, attaining minimum and maximum values of 14° and 48°, respectively (Touma and Wisdom, 1993; Laskar et al., 2004). The concomitant changes in insolation patterns are most pronounced at higher latitudes (Ward, 1992), making the circumpolar PLD particularly susceptible to obliquity variations. Numerous studies have attempted to quantitatively correlate individual PLD layers to martian orbital variations (e.g., Cutts and Lewis, 1982; Laskar et al., 2002; Milkovich and Head, 2004). In this work, we focus upon the larger-scale morphological response of the North Polar Layered Deposits to orbital modulations.

Section 1 summarizes the key topographic observations that must be explained by any evolutionary model of PLD morphology. The kilometer-scale topography of the North PLD is dominated by troughs and scarps—as shown by the Fig. 3 overlay of a Viking Orbiter mosaic upon gridded Mars Orbiter Laser Altimeter (MOLA) data of the North PLD. Despite the high vertical exaggeration (300X), Fig. 3 accurately conveys both (a) the ubiquity of troughs

* Corresponding author. Fax: +1-626-585-1917.
E-mail address: avp@gps.caltech.edu (A.V. Pathare).

0019-1035/$ – see front matter
doi:10.1016/j.icarus.2004.10.030

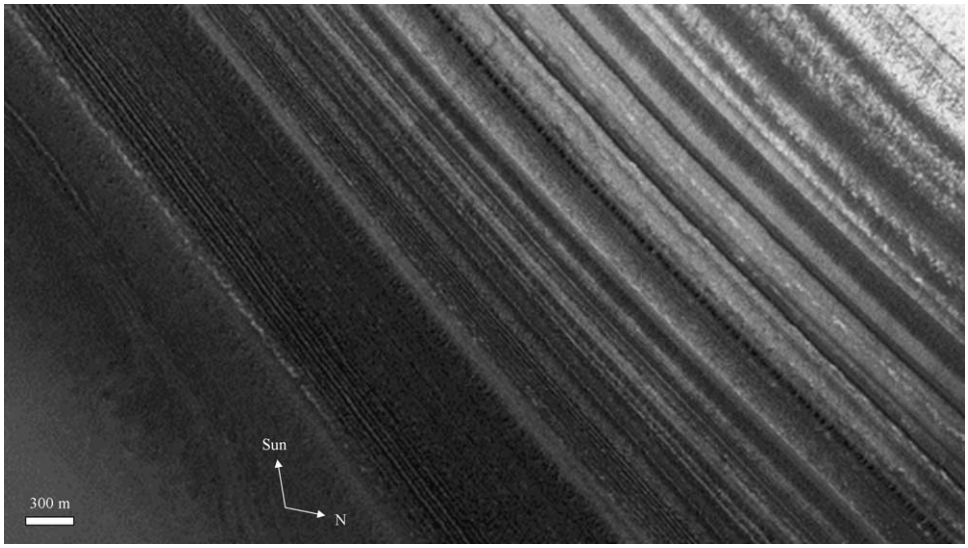

Fig. 1. North Polar Layered Deposits. Portion of MOC Narrow Angle image E01-01092 (13.0 m/pixel, 3.34 km wide) centered at 87.0° N and 264.2° W, showing Layered Terrain within a north polar trough. See Fig. 26A for more of narrow-angle image across entire trough, and Fig. 26B for the wide-angle context image.

throughout the North PLD, and (b) the enhanced steepness of scarps at the margins of the North PLD (e.g., the inner wall of the channel-like reentrant, Chasma Boreale). Most North PLD troughs are asymmetric, with equatorward-facing slopes (α_ε) that are on average 75% steeper than poleward-facing slopes (α_ρ), while primary scarps at the periphery of the North PLD (median $\alpha_\varepsilon = 10.6°$) are generally at least twice as steep as interior troughs. These distinctive topographic features are also important to studies of PLD stratigraphy, since layers are most commonly observed along trough and scarp walls (Thomas et al., 1992). Some fundamental questions regarding PLD morphology that will be addressed in this work include: (1) What mechanism produces trough and scarp topography? (2) How is this mechanism modulated by orbital variations? (3) And what effect does this mechanism have upon PLD stratigraphy?

The most widespread theories of PLD evolution (Howard et al., 1982; Clifford et al., 2000) presume that the asymmetrical slopes of most North PLD troughs ($\alpha_\varepsilon > \alpha_\rho$) result from differential sublimation of water ice driven by the variations in insolation upon the equatorward-facing and poleward-facing trough walls. In Section 2, we integrate the water ice sublimation parameterizations of Ingersoll (1970) into the 1D radiative-convective model of Paige et al. (1994) in order to calculate surface temperatures and sublimation rates, which are first computed for present-day North PLD conditions. We then simulate the effects of orbital variations upon circumpolar surface temperatures and sublimation rates over the last 10 Myr; our results indicate that North PLD sublimation is dominated by high obliquity ($\theta > 32°$) ablation. Our calculations also demonstrate that the insolation upon Sun-facing (at local noon) equatorward-facing trough walls, when integrated over an obliquity "cycle," is not much greater than that incident upon poleward-facing trough walls. Hence we conclude that, contrary to expectations, the steeper equatorward-facing slopes of North PLD trough walls do not result from long-term preferential sublimation driven by variations in incident insolation.

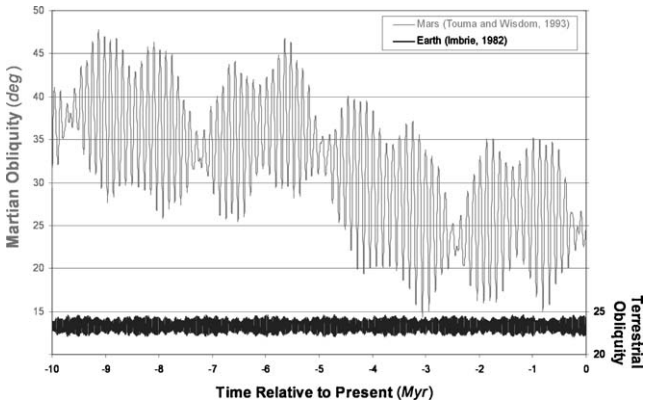

Fig. 2. Martian and terrestrial obliquity. The obliquity histories of Mars (top) and the Earth (bottom) over the last 10 Myr, as calculated by Touma and Wisdom (1993) and Imbrie (1982), respectively. Note that the martian and terrestrial y-axes are offset 10° for clarity.

But then what causes the slope asymmetry of opposing trough walls? We propose that viscous relaxation of subsurface water ice—which as shown in Pathare et al. (2005, this issue) is the modification mechanism most consistent with South PLD crater morphology—may also govern North PLD trough and scarp evolution. In Section 3, we employ the finite element model Tekton (Melosh and Raefsky, 1980) to solve the general viscoelastic equations governing flow within the North PLD. Although Clifford et al. (2000) suggested that the continued presence of North PLD troughs—which rapidly close in terrestrial glaciers due to the higher stresses associated with steeper slopes—argues against flow, our calculated closure times for troughs at present-day martian PLD conditions is on the order of several million years.

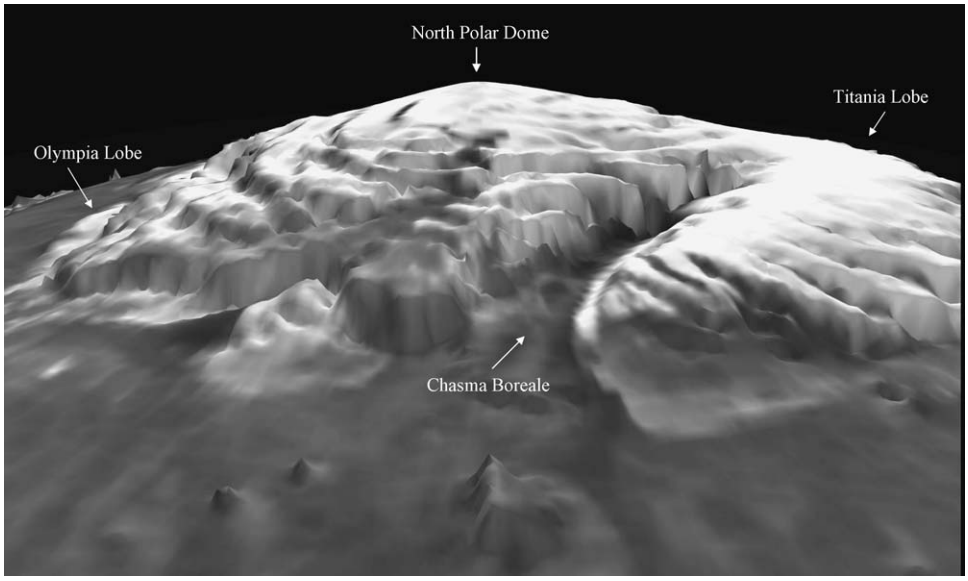

Fig. 3. North PLD morphology. Three-dimensional North PLD overlay of a Viking image mosaic upon MOLA topography, produced and released by the NASA Goddard Space Flight Center Scientific Visualization Studio and the MOLA Science Team. The vertical exaggeration is approximately 300X.

Our finite element simulations indicate that viscous relaxation can explain the strong slope–depth correlation of both North PLD troughs and scarps, an observation that is difficult to reproduce via sublimation or eolian erosion. We also show that a mere 2 K difference in the subsurface temperatures of opposing trough walls is sufficient to produce the observed slope disparity of North PLD troughs, due to the slower rate of uplift of colder poleward-facing trough walls. In Section 4, we suggest that not just the topography but also the stratigraphy of the North PLD is consistent with viscous relaxation, as we theorize that gentle trough-paralleling undulations in Smooth Terrain represent relaxed paleo-troughs. Based on both our sublimation and relaxation modeling, we conclude that present-day North PLD troughs have probably formed since 5 Ma, and are not sites of long-term deposition.

1. PLD topography

1.1. Large scale morphology

In order to constrain evolutionary models of North PLD morphology, we have conducted a thorough examination of the topography of the north polar regions using gridded MOLA altimetry data at 32 pixel/degree resolution (Fig. 4). The spiraling pattern of troughs and scarps is readily apparent in Fig. 4, as is the large arcuate reentrant Chasma Boreale. The main components of the North PLD are a central dome and adjacent lobes, which we have apportioned into four quadrants denoted in Fig. 4 and shown in higher detail in Fig. 5.

The largest component of the North PLD is a parabolic dome with an 1100 × 700 km elliptical base that is centered within 13 km of the pole (Zwally et al., 2000). Since the major axis of this ellipse extends along the 90°–270° W meridian, the North Polar Dome dominates the topography of Quadrants I (Fig. 5A) and III (Fig. 5C). In Quadrant II (Fig. 5B), the thin fan-shaped Olympia Lobe—named for the Olympia Planitia dune fields that mantle much of its surface—abruptly extends from the ∼85° N base of the North Polar Dome out to around 80° N (Zuber et al., 1998; Fishbaugh and Head, 2000). The opposing lobe located in Quadrant IV (Fig. 5D) is much thicker, with a maximum surface relief of 1700 m (Zwally et al., 2000), and gradually descends from the western half of the North Polar Dome (Fig. 3). For simplicity, we will refer to this anti-Olympia Lobe as the "Titania Lobe" (after the mythological precursors and antagonists of the Olympian gods). The prominent reentrant Chasma Boreale separates the Titania Lobe from the eastern half of the North Polar Dome (Fig. 3).

1.2. Mid-scale topography

The spiraling topographic lineations evident in the PLD-wide altimetry maps of Fig. 4 correspond to interior troughs and marginal scarps (Fig. 3). Troughs dominate the kilometer-scale topography of both the North Polar Dome (Figs. 5A, 5C) and the Titania Lobe (Fig. 5B). Steep scarps are present at the periphery of nearly the entire North PLD.

Sample North PLD surface slopes are plotted in Fig. 6, which consists of eight radial profiles spaced at 45° longitudinal intervals through the North PLD. The elevations in Fig. 6 are expressed relative to the mean equatorial radius of Mars (Smith et al., 1999), and are derived from 64 pixel/degree MOLA altimetry grids, allowing for calculation of surface slopes along an approximately 1.6-km long baseline in the radial (i.e., north–south) direction. The relatively wide 45° longitudinal spacing of the Fig. 6 transects minimizes trough and scarp overlap along adjacent profiles (so that the same trough or scarp is not measured

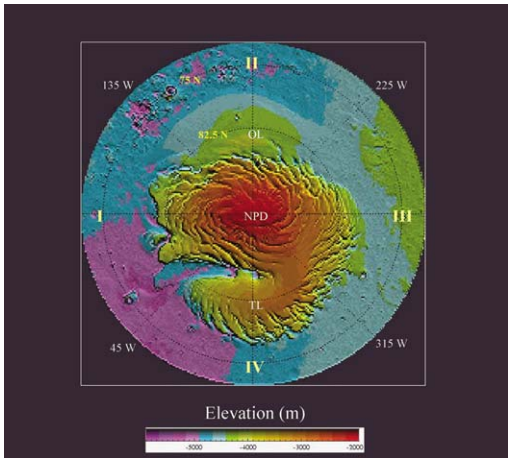

Fig. 4. North PLD topography. Regional MOLA elevation maps (measured relative to the mean equatorial radius: Smith et al., 1999) of the North PLD, created with the MOLA IDL program Gridview (Roark and Frey, 2001) using the global 32 pixel/degree altimetric grid released by the MOLA Science Team. "OL" corresponds to the Olympia Lobe, "NPD" to the North Polar Dome, and "TL" to the Titania Lobe. The roman numerals denote sub-quadrants of the North PLD, which are plotted in Fig. 5.

twice), thereby facilitating a representative survey of the entire North PLD. Along each profile, we have identified all interior troughs and marginal scarps with depths greater than 200 m located between 80° N and 87° N (gridded elevations poleward of 87° N are suspect due to the paucity of MOLA observations at these latitudes). Table 1 summarizes our results: note that the tabulated slopes represent the maximum 1.6-km baseline slope observed along the equatorward-facing walls of troughs and scarps, as well as upon the poleward-facing walls of troughs.

Typical North PLD trough topography is shown by the 90° W profile plotted in Fig. 6B (corresponding to the center line in Fig. 5A), which lies along the major axis of the North Polar Dome. The altimetry of the five inner troughs (labeled "B1"–"B5" in Fig. 6B) exhibits no clear latitudinal dependence, as all have maximum equatorward-facing surface slopes (α_ε) ranging from 2.0° to 4.6° and moderate depths (d) spanning 320 to 470 m (Table 1). In comparison, the outer scarp at the North PLD margin (denoted by "B$") has a much steeper maximum equatorward-facing slope of $\alpha_\varepsilon = 10.5°$ and a significantly greater depth of $d = 710$ m.

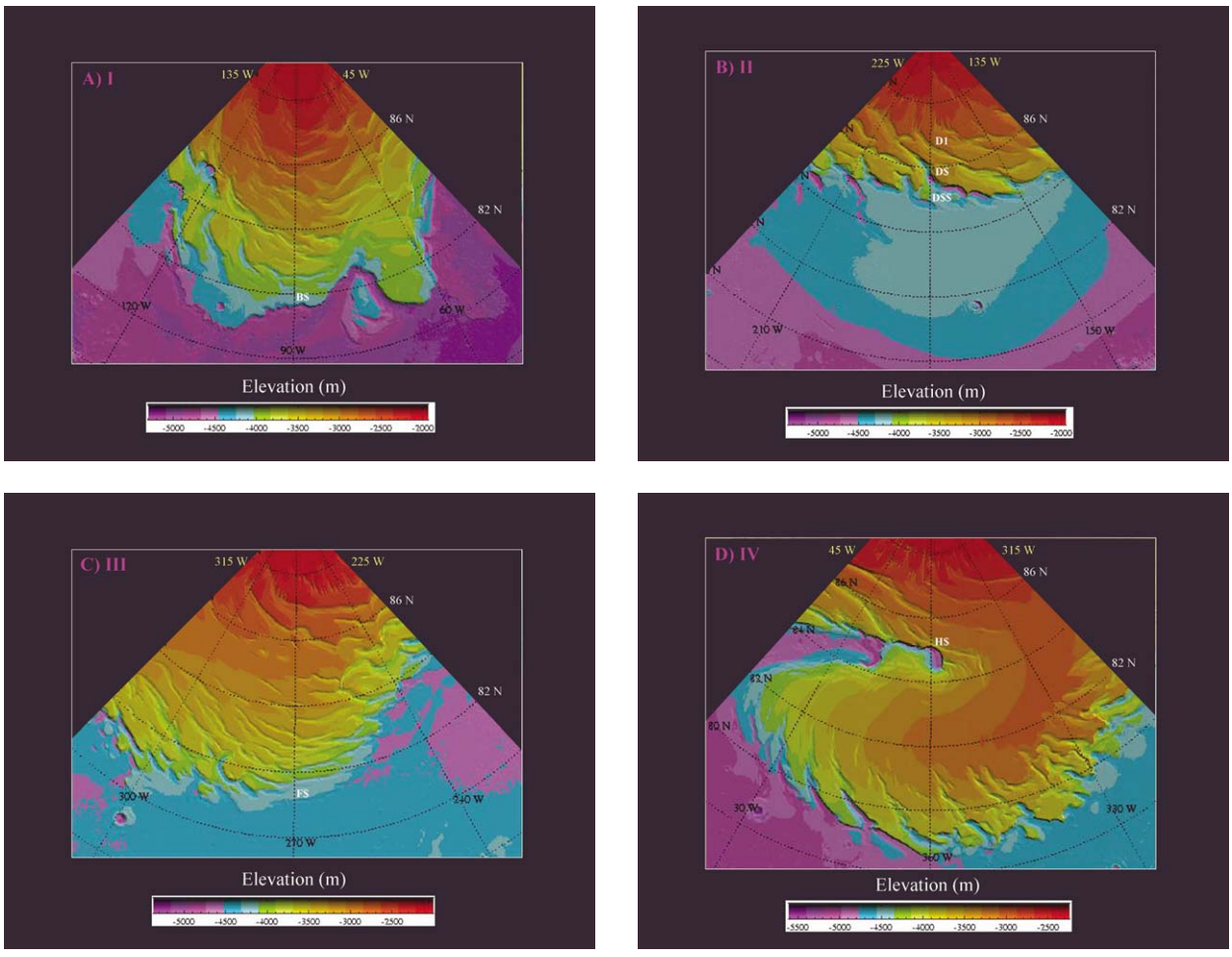

Fig. 5. North PLD quadrant topography. Gridview-created MOLA elevation maps of North PLD Quadrants I–IV (see Fig. 4 for context). The labels {"B$," "D$," "F$," "H$"} in parts {A, B, C, D} indicate primary scarps along {90° W, 180° W, 270° W, 360° W}, which are also denoted in Figs. 6B, 6D, 6F, 6H, respectively. Also shown along 180° W in part (B) are trough "D1" and secondary scarp "D$$" (Fig. 6D).

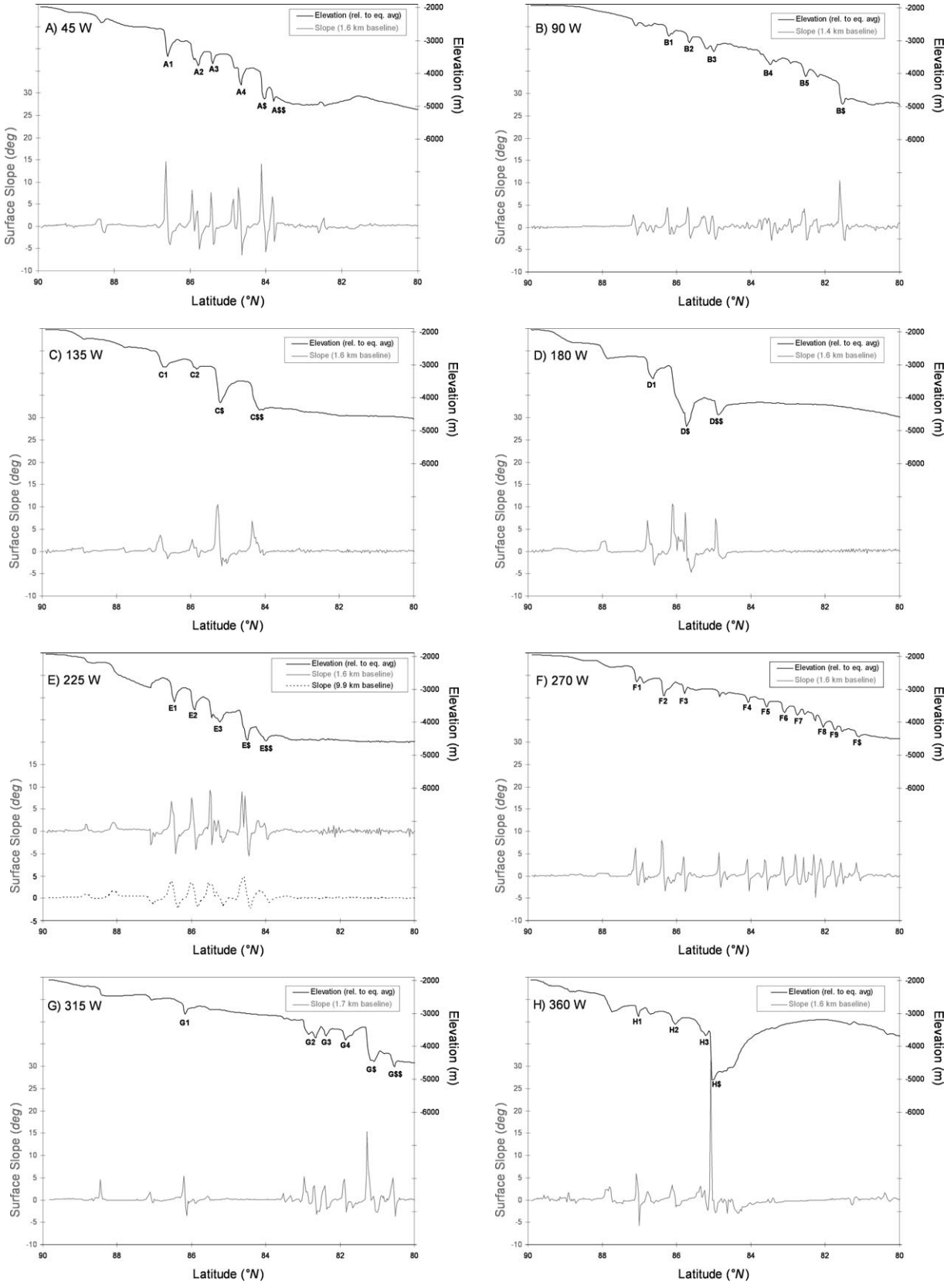

Fig. 6. North PLD profiles. North polar elevations and 1.6-km baseline surface slopes along eight 45° longitudinal increments from 45° W to 360° W, derived from 64 pixel/degree MOLA altimetric grid (see Fig. 5 for context). Alphanumeric labels denote troughs and scarps with minimum surface relief of 200 m (listed in Table 1). Lowermost line in (E) represents surface slopes averaged over a much longer 9.9-km baseline, which is slightly offset for clarity.

Table 1
North PLD troughs and scarps

Feature	Long (° W)	Lat (° N)	EWF slope	PWF slope	Ratio	Base	Depth	Environs	Thickness
Troughs									
A1	45	86.6	14.5	−4.1	3.5	−3481	844	−4960	2323
A2	45	85.9	8.1	−5.3	1.5	−3761	725	−4960	1924
A3	45	85.4	7.6	−4.2	1.8	−3702	371	−4960	1629
A4	45	84.7	8.7	−6.4	1.4	−4354	906	−4960	1512
B1	90	86.2	4.4	−1.5	2.9	−2860	324	−4940	2404
B2	90	85.7	4.6	−2.5	1.8	−3066	322	−4940	2196
B3	90	85.0	2.6	−2.6	1.0	−3331	430	−4940	2039
B4	90	83.5	2.0	−3.0	0.7	−3732	446	−4940	1654
B5	90	82.6	4.2	−2.8	1.5	−4076	389	−4940	1253
C1	135	86.8	3.6	−1.6	2.2	−3068	474	−4700	2106
C2	135	86.0	2.7	−1.3	2.1	−3131	274	−4700	1843
D1	180	86.8	7.0	−3.1	2.2	−3412	618	−4870	2076
E1	225	86.5	6.8	−5.0	1.4	−3390	676	−4610	1896
E2	225	86.0	7.5	−4.2	1.8	−3609	616	−4610	1617
E3	225	85.5	9.2	−2.6	3.6	−3993	743	−4610	1360
F1	270	87.1	6.3	−2.1	3.0	−2813	480	−4500	2167
F2	270	86.4	8.0	−3.4	2.4	−3194	518	−4500	1824
F3	270	85.8	4.3	−3.5	1.2	−3133	279	−4500	1646
F4	270	84.1	3.8	−3.4	1.1	−3397	208	−4500	1311
F5	270	83.6	3.7	−3.2	1.1	−3519	226	−4500	1207
F6	270	83.2	4.4	−2.2	2.0	−3711	321	−4500	1110
F7	270	82.8	4.9	−1.9	2.5	−3782	265	−4500	983
F8	270	82.1	3.9	−2.6	1.5	−4149	323	−4500	674
F9	270	81.8	3.3	−2.4	1.4	−4233	237	−4500	504
G1	315	86.2	5.4	−3.5	1.6	−3027	384	−4625	1982
G2	315	83.0	5.3	−3.2	1.7	−3741	551	−4625	1435
G3	315	82.4	3.3	−2.1	1.6	−3621	222	−4625	1226
G4	315	81.9	4.7	−2.7	1.7	−3816	308	−4625	1117
H1	360	87.1	5.9	−5.8	1.0	−3103	353	−5010	2260
H2	360	86.1	3.4	−1.5	2.3	−3336	322	−5010	1996
H3	360	85.4	3.1	−2.3	1.3	−3672	398	−5010	1736
Primary scarps									
A$	45	84.1	14.1	–	–	−4773	874	–	874
B$	90	81.6	10.5	–	–	−4925	711	–	711
C$	135	85.3	10.5	–	–	−4158	1081	–	1081
D$	180	86.1	10.7	–	–	−4868	1824	–	1824
E$	225	84.6	8.8	–	–	−4525	892	–	892
F$	270	81.2	3.0	–	–	−4446	208	–	208
G$	315	81.3	15.2	–	–	−4449	1035	–	1035
H$	360	85.1	31.5	–	–	−5006	1423	–	1423
Secondary scarps									
A$$	45	83.8	6.6	–	–	−4849	440	–	440
C$$	135	84.3	6.9	–	–	−4365	838	–	838
D$$	180	84.9	7.3	–	–	−4516	427	–	427
E$$	225	84.2	2.4	–	–	−4573	431	–	431
G$$	315	80.6	5.0	–	–	−4619	397	–	397

Morphological properties of North PLD interior troughs and marginal scarps with a minimum depth of 200 m located between 80° N and 87.3° N along the eight topographic transects (A–H) plotted in Fig. 6. "Equatorward-facing slope" and "poleward-facing slope" represent maximum wall slopes along approximate ∼1.6-km baseline slope. Total PLD thickness is computed by subtracting the average off-North PLD elevation along a given meridian ("environs") from the elevation of the trough or scarp crest. A typical PLD thickness for interior troughs is 2 km, which is employed as the nominal value for the relaxation simulations of Section 3 (note that by definition thicknesses for scarps are equivalent to depths).

Note that the term "scarp" is not meant to indicate formation of a steep slope via erosion of highly resistant rocks, as is often implied in terrestrial usage.

Instead, we classify "B$" as a "scarp" simply based on the penetration of its floor to the approximate average elevation (in this case, −4900 m) of the local circum-North PLD terrain. Hence, even though the profile of "B$" is superficially trough-like, it differs from the interior troughs (B1–B5) in that the base of the outer poleward-facing wall is not physically connected by PLD material to the base of the inner equatorward-facing wall (as is readily apparent in Fig. 5A). The reason this distinction is so important is that as shown in Section 4 the effects of viscous relaxation upon a depression whose floor is more rigid than its walls are com-

pletely different from the rheological response of a trough in which the floor and walls are comprised of the same material.

The complexities of typical North PLD scarp topography are illustrated in Fig. 6D by the 180° W profile situated along the minor axis of the North Polar Dome (Fig. 5B). There is only one interior trough ("D1") along this profile, yet there are *two* marginal scarps ("D$" and "D$$"). As shown in Fig. 5B, the presence of inner primary ("D$") and outer secondary ("D$$") marginal scarps results from the large-scale spiral pattern of North PLD topography. The smaller ($d = 780$ m, $\alpha_\varepsilon = 7.3°$) outer scarp "D$$" descends well below the Olympia Lobe that it dissects, while the more prominent ($d = 1820$ m, $\alpha_\varepsilon = 10.7°$) inner scarp "D$" clearly penetrates below the average ~4500 m elevation at the boundary of Olympia Planitia (Figs. 5B, 6D). That "D$" and other similar primary scarps (Figs. 6A, 6C, 6E, 6G) are definitively not troughs is an important point to emphasize, since we suspect that conflation of trough and scarp morphology has led some previous workers to suggest that North PLD troughs increase in steepness and depth with increasing distance from the pole (e.g., Howard, 2000).

However, our profile-based analysis of North PLD troughs reveals little correlation of topography with latitude. Figure 7A plots the latitudinal dependence of maximum surface slopes along the walls of all of the North PLD troughs and scarps listed in Table 1. Neither maximum equatorward-facing trough wall slopes (filled circles) nor poleward-facing trough wall slopes (open circles) increase with polar colatitude—in fact, equatorward-facing trough slopes are slightly greater closer to the pole (>85° N). Figure 7A reflects the asymmetrical nature of North PLD troughs: of the 31 troughs identified, 28 have steeper equatorward-facing walls, 2 are symmetrical ("B3" at 85.0° N and "H1" at 87.1° N), and only 1 has a steeper poleward-facing wall ("B4" at 83.5° N). Overall, we find that maximum equatorward-facing trough slopes range from 2.0°–14.5° while maximum poleward-facing trough slopes span 1.3°–6.4°, which is consistent with the range of North PLD trough slopes reported by Zwally et al. (2000). Additionally, we calculate mean maximum equatorward-facing and poleward-facing trough slopes of $\alpha_\varepsilon = 5.4°$ and $\alpha_\rho = 3.1°$, which are in excellent agreement with the typical values of $4° < \alpha_\varepsilon < 7°$ and $2° < \alpha_\rho < 4°$ reported by Ivanov and Muhleman (2000), as well as the more comprehensive analysis conducted by Nomanbhoy et al. (2004).

Figure 7A also shows that the maximum surface slopes of primary scarps (large triangles) at the margins of the North PLD are generally much greater (median $\alpha_\varepsilon = 10.6°$) than analogous equatorward-facing trough slopes. However, the outermost secondary scarps (small triangles), which have a mean maximum slope of $\alpha_\varepsilon = 5.6°$, are not significantly steeper than equatorward-facing trough walls. As shown in Fig. 7B, primary scarps are also much deeper (mean depth $d = 1010$ m) than both interior troughs (mean $d = 440$ m) and secondary scarps (mean $d = 510$ m). Primary scarp

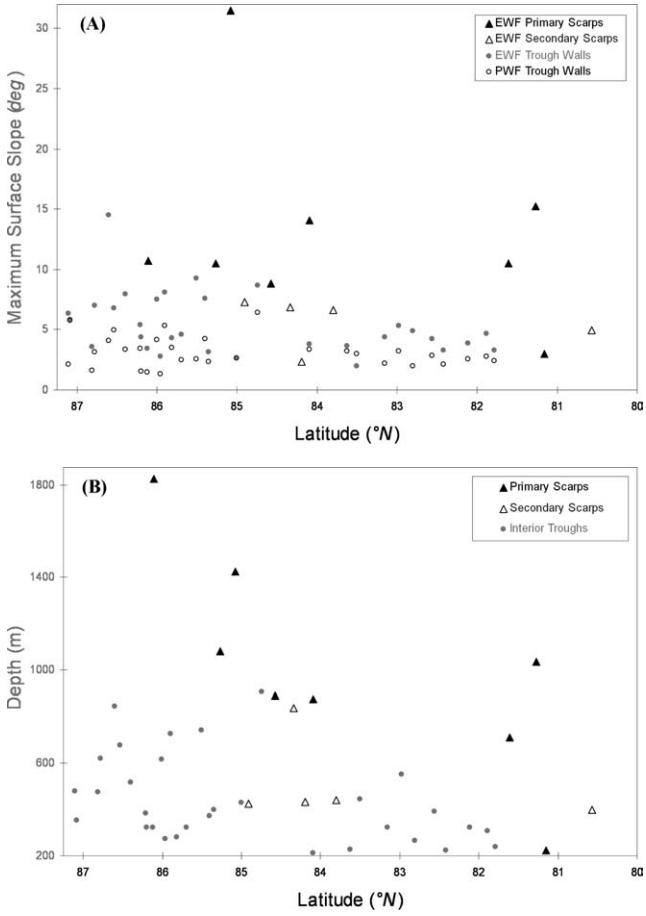

Fig. 7. North PLD slopes and depths vs. latitude. Parts (A) and (B) plot latitudinal dependence of North PLD trough and scarp maximum surface slope and total depth (respectively), the values of which are listed in Table 1. All surface slopes are calculated over an approximate 1.6-km baseline.

depth is correlated with latitude, which is of course expected since scarps closer to the pole must be deeper in order to penetrate through the locally-thicker deposits to the sub-PLD basement (and thus be classified a "scarp"). Average trough depths are also slightly elevated poleward of 85° N, much like maximum equatorward-facing trough slopes (Fig. 7A). However, inspection of the seven deepest troughs listed in Table 1 reveals that six are located along the 45° W–225° W meridian (Figs. 6A, 6E), indicating that North PLD trough topography exhibits more of a longitudinal association than a latitudinal correlation. Consequently, there is no significant dependence of maximum trough slope or total trough depth upon latitude.

However, North PLD trough slopes and depths are strongly correlated with one another. Figure 8 plots maximum equatorward-facing wall slopes versus total depth for both troughs (circles) and scarps (triangles). Trough slopes and depths are characterized by a correlation of $R_c = 0.78$, while scarp slopes and depths exhibit a somewhat lower correlation of $R_c = 0.65$ (removal of the two scarp outliers increases R_c to 0.81). Thus we find that the most significant correlation involving North PLD morphology, for both

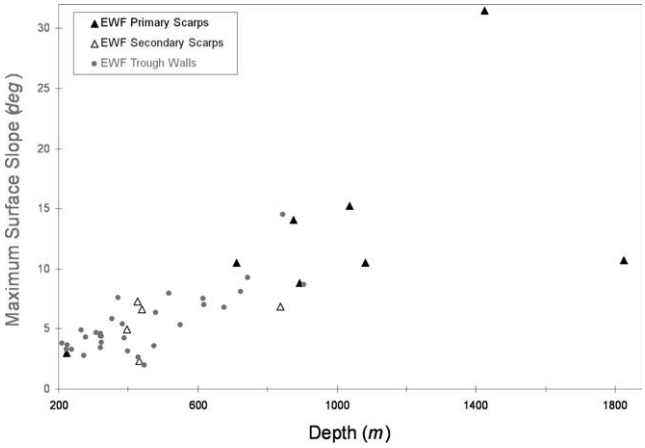

Fig. 8. North PLD slopes vs. depths. Dependence of the maximum surface slopes of North PLD trough and scarp walls upon total depth, the values of which are listed in Table 1. The slope–depth correlation is characterized by $R_c = 0.78$. All surface slopes are calculated over an approximate 1.6-km baseline.

troughs and scarps, is that between maximum surface slopes and total depth (Fig. 8).

1.3. Key questions

In summary, evolutionary models of PLD morphology must address the following questions concerning the topography of the North PLD:

(1) Why are most troughs asymmetric, with maximum equatorward-facing slopes (mean $\alpha_\varepsilon = 5.4°$) that are on average 75% steeper than maximum poleward-facing slopes (mean $\alpha_\rho = 3.1°$)?
(2) Why are primary scarps (median $\alpha_\varepsilon = 10.6°$) generally steeper than the equatorward-facing slopes of interior troughs, but not secondary scarps (mean $\alpha_\varepsilon = 5.6°$)?
(3) And lastly, why are maximum surface slopes and total depths so strongly correlated for both troughs and scarps?

2. North PLD sublimation

2.1. Sublimation model

Ingersoll (1970) established the basic theory of water ice sublimation on Mars, which can result from either buoyant convection of a thin H_2O-saturated near-surface layer that is lighter than the above unsaturated CO_2-dominated ambient atmosphere, or turbulent mixing by local winds of this saturated near-surface layer with the overlying atmosphere. Ingersoll (1970) formulated the following now-standard parameterizations for the mass flux of water vapor above an ice deposit for both buoyancy-driven (E_b) and turbulence-driven (E_t) sublimation:

$$E_b = 0.17 D \rho_w (1-r)\left[(\Delta\rho/\rho_a) g/\nu^2\right]^{1/3}, \quad (1a)$$

$$E_t = 0.002 w \rho_w (1-r), \quad (1b)$$

where D is the diffusion coefficient of water vapor in carbon dioxide, ρ_a is the total atmospheric gas density, $\Delta\rho$ is the difference between the total atmospheric gas density and that of the saturated gas at the surface, g is the martian gravitational acceleration, ν is the kinematic viscosity of carbon dioxide, and w is the wind speed 1 m above the surface (Haberle and Jakosky, 1990). Both sublimation mechanisms depend on the relative humidity r—the closer the ambient atmosphere already is to saturation ($r = 1$), the lower the rate of sublimation—and the temperature T_s of the ice surface. The thermal dependence is expressed through the saturation water vapor density $\rho_w = \rho_a \times \varepsilon_m \times (e/P)$, for atmospheric pressure P, molecular weight mass ratio $\varepsilon_m = M_{H_2O}/M_{CO_2}$, and saturation water vapor pressure $e = a_o \exp(-b_o/T_s)$, where a_o and b_o are constants. Thus the total mass flux $(E_b + E_t)$ is an exponential function of surface temperature.

We have implemented the above sublimation parameterizations (Eq. (1)) into the Paige et al. (1994) one-dimensional radiative-convective model of polar surface temperatures, which solves the heat balance between incident insolation, atmospheric heating, radiative cooling, sublimation losses, and subsurface conduction via the surface boundary condition:

$$\varepsilon_s \sigma T_s^4 = F_s(1-a) + F_a - E_v L_v - K(\partial T/\partial z), \quad (2)$$

where ε_s is the surface emissivity, σ is the Stefan–Boltzmann constant, F_s is the incident solar flux, a is the surface albedo, F_a is the infrared heating flux due to the atmosphere, E_v is the net sublimation rate for a given volatile (either CO_2 or H_2O), L_v is the latent heat of sublimation of that volatile, and K is the thermal conductivity.

The incident insolation at the surface depends upon a variety of factors, including obliquity (θ), eccentricity (e), argument of perihelion (ω), surface slope (α), latitude, and season (L_s). (Note that martian orbital longitude values of $L_s = 0°/90°/180°/270°$ correspond to vernal equinox/summer solstice/autumnal equinox/winter solstice in the northern hemisphere.) The effects of CO_2 gas absorption and dust scattering upon the downward solar flux F_s are also considered (Paige et al., 1994), using Mie properties derived by Tomasko et al. (1999) from Mars Pathfinder observations of atmospheric dust. The downward infrared flux F_a is calculated by considering CO_2 emission and absorption in the strong 15-μm band, infrared dust scattering and emission outside of this band, and conductive and convective heat transport between the atmosphere and surface (Paige et al., 1994). The near-surface thermal profile ($\partial T/\partial z$) varies with the conductivity (K), density (ρ), and heat capacity (c), which are encapsulated by the composite quantity thermal inertia $I_{th} = \sqrt{K\rho c}$ (Paige et al., 1994).

The sublimation of carbon dioxide ice depends upon insolation, as well as CO_2 frost albedo and emissivity. We assume that sublimation of water ice, as prescribed by Eq. (1), does not occur until the seasonal CO_2 frost cap has

completely sublimated away, since H_2O sublimation rates are negligible at typical CO_2 frost point temperatures of ~148 K. Although the atmospheric model of Paige et al. (1994) is one-dimensional, we have incorporated a diurnal advection efficiency parameter ε_{adv} that is equal to the rate at which an atmospheric column of water vapor is removed by horizontal advection. For example, if the entire H_2O column over a no-longer sublimating ice surface is laterally displaced over the course of exactly one martian day (or sol), then $\varepsilon_{adv} = 1$; if it takes 4 sols to advect away this column, then $\varepsilon_{adv} = 0.25$. Maximum water ice sublimation rates result from total instantaneous advection ($\varepsilon_{adv} = \infty$), since in this idealized scenario the relative humidity is always zero ($r = 0$).

2.2. Present-day observations

The sublimation rate of North PLD water ice is constrained by Viking Mars Atmospheric Water Vapor Detector (MAWD) observations, which are plotted in Fig. 9 as a function of latitude and season. Columnar water vapor abundances in the northern hemisphere exhibit a dramatic rise at the beginning of northern summer, shortly after the exposure of North PLD water ice due to complete defrosting of the seasonal CO_2 cap (Jakosky and Farmer, 1982). MAWD did not detect a similar increase in circum-South PLD water vapor abundance during southern summer, presumably because of the perennial presence of the carbon dioxide South Polar Cap (Jakosky and Haberle, 1992).

The MAWD-observed northern hemispheric water vapor increase of 7×10^{11} kg places an upper limit on net summertime sublimation across the North PLD (Haberle and Jakosky, 1990). However, both the 2D transport model of Haberle and Jakosky (1990) and the 3D Mars General Circulation Model (GCM) of Richardson (1999) predict that only about 40% of this northern hemispheric water vapor increase is attributable to sublimation from the North PLD, suggesting a net summertime mass loss of 2.8×10^{11} kg. For

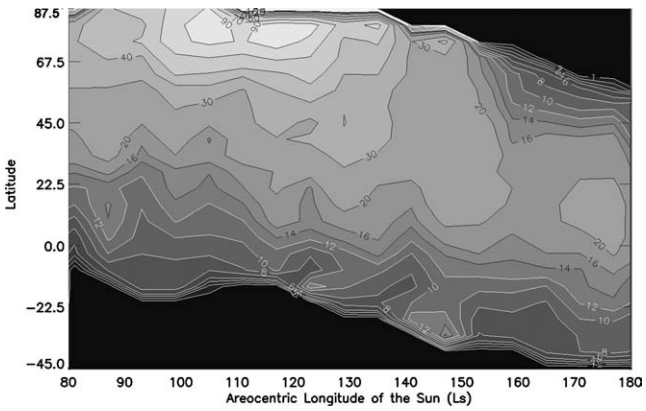

Fig. 9. Martian water vapor abundance during northern summer (pr. μm). Latitudinally-binned Viking MAWD observations of columnar water vapor (expressed as precipitable microns) collected during northern summer of the second year of *Viking Orbiter* operations.

comparison, Zuber et al. (1998) estimate that the North PLD, with a mean surface relief of 1030 m over a 1.04×10^6 m^2 surface area, could contain as much as 1.4×10^{18} kg of water ice. So if the net sublimation flux lost during the summer of each martian year is permanently removed from the north polar regions, then the entire North PLD would be eradicated by sublimation losses in just $t = 1.4 \times 10^{18}/2.8 \times 10^{11} = 5 \times 10^6 \times (1.88 \text{ Earth years}/(\text{Mars year})) = 9.4$ Myr.

However, Mars GCM models predict that most if not all of the summertime sublimated water vapor eventually returns to the North PLD the following winter, after first recondensing in the northern seasonal CO_2 frost cap (Houben et al., 1997; Richardson, 1999). Although this return flux of H_2O is commonly presumed to redistribute itself more or less evenly across the entire North PLD (Clifford et al., 2000), an alternative scenario is suggested by the modeling of Houben et al. (1997). According to their GCM simulations, most of the water vapor that sublimates from the retreating edge of the seasonal CO_2 cap is driven poleward by baroclinic eddies, leading to subsequent recondensation of H_2O within the CO_2 frost still present at higher latitudes. This process continues repeatedly until the shrinking seasonal CO_2 cap completely evaporates, resulting in the large-scale recondensation of water vapor close to the center of the North PLD (Houben et al., 1997).

Bass and Paige (2000) provide observational support for this "vacuuming" of water vapor towards the north pole. Using contemporaneous Viking Infrared Thermal Mapper (IRTM) and MAWD observations, Bass and Paige (2000) show that a large water vapor pulse is released into the circum-North PLD atmosphere only after the central regions poleward of 85° N have defrosted (even though peripheral North PLD temperatures are substantially warmer). As polar temperatures decrease later in the summer, the darker margins of the North PLD exhibit a gradual increase in albedo, a brightening that is consistent with fresh condensation of water ice at the surface (Bass et al., 2000). However, Bass and Paige (2000) find that the center of the North PLD is always brighter than the margins, which suggests that the central regions may be zones of net H_2O accumulation.

As for ablation, the north polar albedo maps of Paige et al. (1994) derived from Viking IRTM observations suggest that sublimation of water ice is not occurring throughout the entire North PLD. As shown in Fig. 10, the latitudinally-averaged apparent albedo (lower solid line) between 89° N and 90° N is $a = 0.45$, well within the $0.34 < a < 0.51$ range of actively sublimating "clean ice" in terrestrial glaciers (Paterson, 1994). Yet between 80° N and 81° N the average albedo falls to $a = 0.25$, which is at the upper end of so-called "dirty ice" that may or may not be undergoing sublimation (Paterson, 1994). For example, the extremely low albedo dunes ($a = 0.15$) of Olympia Planitia are clearly not sublimating (Thomas et al., 1992); additionally, Haberle and Jakosky (1990) conclude from their analysis of MAWD data that the dark ($a \sim 0.25$) spiral lanes within the North PLD

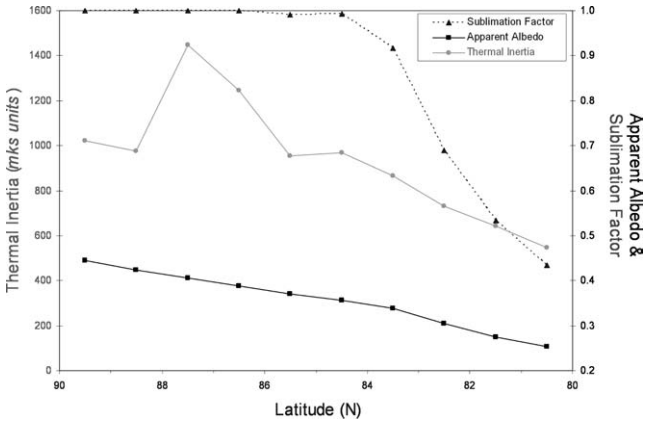

Fig. 10. North PLD surface properties. Latitudinal dependence of thermal inertia ($J/(m^2\,s^{-1/2}\,K)$) and apparent albedo, as averaged in one degree wide latitude bands from the IRTM-derived polar maps of Paige et al. (1994). The sublimation factor refers to the portion of each latitude band with albedo above $a = 0.30$, which we assume to be the minimum albedo of actively sublimating water ice.

(Fig. 3) corresponding to equatorward-facing trough walls cannot be actively sublimating.

For simplicity, we assume that sublimation of water ice only occurs within relatively bright $a > 0.30$ albedo regions of the North PLD. As shown by the dashed line in Fig. 10, this minimum albedo criterion results in an areal sublimation factor (f_{sub}) that varies from essentially 100% poleward of 84° N to as low as $f_{sub} = 0.43$ between 80° N and 81° N. Overall, the fractional sublimation factor for the entire North PLD is $f_{sub} = 0.75$, resulting in an effective North PLD sublimating surface area of $0.75 \times 1.04 \times 10^{12}\ m^2 = 7.8 \times 10^{11}\ m^2$.

We define the effective annual North PLD sublimation loss rate E_{net} as the net summertime mass loss divided by the effective surface area: $E_{net} = 2.8 \times 10^{11}$ kg/7.8×10^{11} m^2 per martian year = 0.36 kg/m^2 per 1.88 Earth years = 0.19 kg/(m^2 yr). Note that this definition does not include the aforementioned advection of water vapor *back* to the North PLD via wintertime recondensation. Since 1 kg of H_2O per square meter is equivalent to a 1 mm thick layer of precipitated water, the net annual North PLD sublimation loss rate can be expressed as $E_{net} = 0.19$ pr. mm/yr.

2.3. Present-day simulations

We first run our water ice sublimation model for input parameters appropriate to average North PLD conditions in order to verify that our predicted sublimation rates are consistent with MAWD water vapor observations. The present-day orbital configuration of Mars is characterized by $\theta = 25.2°$, $e = 0.093$, and $\omega = 251°$ (i.e., perihelion passage occurs at $L_s = 251°$, or near southern summer solstice). As for the atmosphere, MOLA altimetry of the North PLD correspond to an average surface pressure of $P = 7$ mbar (Zuber et al., 1998), Thermal Emission Spectrometer (TES) observations indicate a typical North PLD opacity of $\tau = 0.1$ (Smith et al., 2001), and the dynamical modeling of Haberle and Jakosky (1990) suggest a mean near-surface wind speed of $w = 10$ m/s. Following Paige et al. (1994), we assume unit emissivities for both water ice and carbon dioxide frost, as well as a CO_2 frost albedo of 0.55, which best fits the observed seasonal behavior of the north polar seasonal cap (Paige and Ingersoll, 1985).

We simulate an untilted ($\alpha = 0°$) surface in the middle of the North PLD at 85° N, calculating surface temperatures and sublimation rates at least once every martian hour for an entire Mars year. Since we are only concerned with the fraction (f_{sub}) of the North PLD that is undergoing sublimation, we derive average albedo and thermal inertia values of $a = 0.38$ and $I_{th} = 900$ J/(m^2 s$^{1/2}$ K) from the North PLD maps of Paige et al. (1994) based only upon the 75% of the North PLD that exceeds our minimum albedo criterion of $a > 0.3$. For these averaged present-day North PLD conditions, our model predicts an annual average surface temperature at 85° N of $T_{sav} = 162$ K. Surface temperatures are so low because the North PLD is blanketed by CO_2 at its 7 mbar frost point of 148 K for most of the year: once the last of the carbon dioxide sublimates away slightly before $L_s = 90°$, temperatures rapidly increase, reaching a maximum of 220 K near $L_s = 110°$. Our predicted present-day North PLD surface temperatures are consistent with those derived from IRTM measurements by Paige et al. (1994), which is of course to be expected since many of our input parameters and model techniques are based upon that work.

Of greater significance are our corresponding present-day North PLD sublimation results. As shown in Fig. 11, the diurnal advection efficiency parameter ε_{adv} controls both the net annual sublimation (E_{net}) and the maximum columnar water vapor abundance (W_{max}). If there is no advection ($\varepsilon_{adv} = 0$), then $E_{net} = 0$, since all of the water ice that sublimates remains within the local atmospheric column ($W_{max} = 106$ pr. μm = 0.106 pr. mm) and then recondenses. But if $\varepsilon_{adv} = 1$, then substantially more sublimation occurs ($E_{net} = 1.26$ pr. mm/yr) due to the much lower relative humidities. The MAWD-derived North PLD sublimation loss rate of $E_{net} = 0.19$ pr. mm/yr corresponds to an advection efficiency of $\varepsilon_{adv} = 0.05$—which notably also produces maximum water vapor abundances of $W_{max} = 87$ pr. μm that are in excellent agreement with north polar MAWD observations (as indicated by the "+" marks in Fig. 9). Hence we conclude that our model accurately simulates the present-day sublimation of North PLD water ice.

2.4. Obliquity-dependent sublimation

We now consider the effects of orbitally-induced changes in surface temperatures upon sublimation rates, which will be especially pronounced in the martian polar regions (Toon et al., 1980). Incident insolation depends on three orbital parameters (Ward, 1992): obliquity (θ), which determines the solar elevation angle seen on the planet; eccentricity (e), which controls the solar distance of the planet; and argument

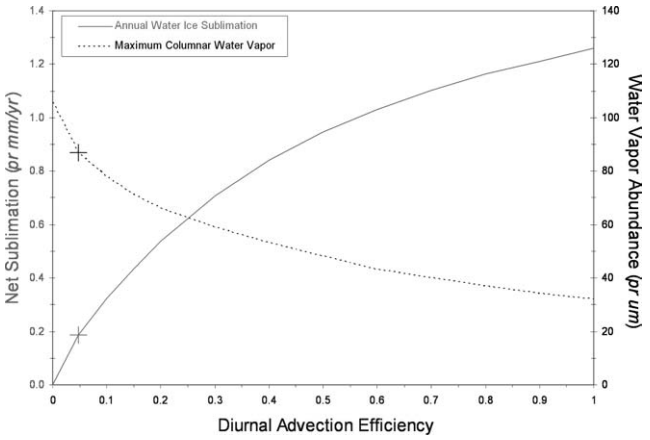

Fig. 11. Present-day North PLD sublimation. Dependence of net annual sublimation and maximum columnar water vapor abundance upon the diurnal advection efficiency parameter, for the present-day orbital configuration ($\theta = 25.2°$, $e = 0.09$, $\omega = 251°$) and otherwise nominal North PLD conditions (enumerated in Table 2). The "+" marks denote the values corresponding to the advection efficiency ($\varepsilon_{adv} = 0.05$) that best fits the MAWD-derived sublimation rate and MAWD-observed water vapor abundance.

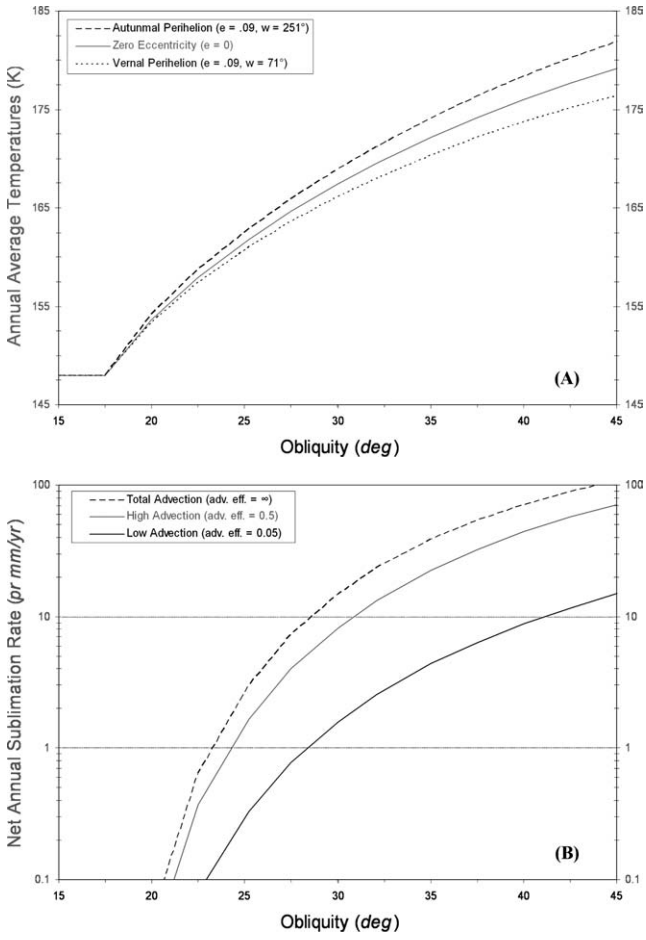

Fig. 12. Obliquity-modulated North PLD variations. (A) Dependence of annual average surface temperature upon obliquity, for three different orbital configurations and otherwise nominal North PLD conditions. (B) Dependence of net annual sublimation rate upon obliquity, for three different diurnal advection efficiencies and otherwise nominal North PLD conditions (Table 2).

of perihelion (ω), which affects the phasing of the solar elevation angle with solar distance in the planet's orbit. Mars experiences significant fluctuations to all three of these parameters.

Touma and Wisdom (1993) showed that martian obliquity varies chaotically due to a secular spin–orbit resonance, ranging from 14° to 48° over the last 10 Myr, with a median value of $\theta = 32.1°$ that is well above the present-day $\theta = 25.2°$ (Fig. 2). Touma and Wisdom (1993) noted that their recent obliquity history is "remarkably similar" to the quasiperiodic calculations of Ward and Rudy (1991), who also predicted the onset of a significant increase in mean martian obliquity approximately 4 Ma. Similarly, Laskar et al. (2004) have recently predicted an obliquity history which over the last 10 Myr is quite similar to that of Touma and Wisdom (1993), although Laskar et al. (2004) do predict significantly higher average obliquities prior to 10 Ma.

Martian obliquity variations are extremely rapid—typically, the value of θ stays within 5° of itself for less than 10,000 yr (Fig. 2). Exceptions to this rule of thumb occur every 2–3 Myr during "node" transitions in which θ oscillations are significantly damped: Mars is now in such a transitional node. Martian eccentricity undergoes a quasiperiodic 0.04 magnitude variation every 100,000 yr superimposed upon a larger 0.1 magnitude variation every 2 Myr: the minimum $e = 0$, and the current $e = 0.093$ is close to the maximum value of $e = 0.1$ (Ward, 1992). The argument of perihelion is presently $\omega = 251°$, and cycles with an approximate 50,000 yr period (Ward, 1992).

Figure 12A shows the results of subjecting the nominal North PLD surface and atmosphere conditions described in Section 2.3 (e.g., $a = 0.38$ and $\varepsilon_{adv} = 0.05$) to the full range of martian orbital configurations. For the present-day eccentricity of $e = 0.093$ and late autumnal perihelion ($\omega = 251°$), increasing the obliquity from the current $\theta = 25.2°$ to $\theta = 45°$ raises annual average surface temperatures in the North PLD from $T_{sav} = 162$ K to $T_{sav} = 182$ K (upper dashed line). Although shifting the timing of perihelion to late northern spring ($\omega = 71°$) results in *maximum* summertime North PLD surface temperatures of 270 K (for $\theta = 45°$ and $e = 0.093$), annual average North PLD surface temperatures for this scenario (lower dashed line) are actually less than for autumnal perihelion passage, due to the comparatively shorter summers. At a given θ, our modeling indicates that a zero eccentricity circular orbit results in median surface temperatures (solid line) for that obliquity—and therefore also median sublimation rates. Hence for the remainder of this work we adopt $e = 0$ (for which ω is undefined due to the lack of a single perihelion) as the nominal eccentricity for our obliquity-dependent calculations.

Figure 12B depicts the dependence of North PLD sublimation rates upon obliquity and diurnal advection. For a low advection efficiency of $\varepsilon_{adv} = 0.05$ (solid line), we compute a net annual sublimation loss rate of $E_{net} = 15$ pr. mm/yr at

45° obliquity. Since circumpolar circulation may be more vigorous at higher obliquities (Jakosky and Carr, 1985; Richardson, 1999), we also consider a high advection scenario with $\varepsilon_{adv} = 0.5$ (long-dashed line), obtaining $E_{net} = 71$ pr. mm/yr at $\theta = 45°$, which is close to the theoretical maximum loss rate for $\theta = 45°$ of $E_{net} = 108$ pr. mm/yr associated with total instantaneous advection ($\varepsilon_{adv} = \infty$: short-dashed line).

Our results are consistent with those of Jakosky et al. (1995), who assumed idealized sublimation into a perpetually dry atmosphere (i.e., $r = 0$, $\varepsilon_{adv} = \infty$), and for analogous $\theta = 45°$ conditions calculated a net annual North PLD sublimation rate of $E_{net} \sim 100$ pr. mm/yr. Regardless of the efficiency of advection, our calculations indicate that near-maximum $\theta = 45°$ North PLD sublimation rates are approximately two orders of magnitude greater than the corresponding $\theta = 25.2°$ values of E_{net} (Fig. 12B). Even at the median obliquity since 10 Ma of $\theta = 32.1°$, predicted sublimation rates are still over 10 times greater than current North PLD loss rates.

Therefore, the long-term sublimation of the North PLD must be dominated by losses at high obliquities—as demonstrated by Fig. 13A, which plots the fractional amount of total North PLD sublimation over the last 10 Myr corresponding to a given obliquity range (assuming the recent martian obliquity history shown in Fig. 2). Less than 1% of the total North PLD sublimation since 10 Ma has occurred at or below the present $\theta = 25.2°$ obliquity; in contrast, more than 80% of North PLD losses during this time have taken place at obliquities greater than the median value of $\theta = 32.1°$. Due to the sudden rise in mean obliquity circa 4 Ma, the obliquity sensitivity of sublimation rate produces a temporal partitioning of sublimation: as shown in Fig. 13B, less than 12% of the total amount of North PLD sublimation since 10 Ma has occurred in the last 4 Myr. Consequently, we conclude that evolutionary models of North PLD morphology must explicitly consider obliquity-induced variations in water ice sublimation rates.

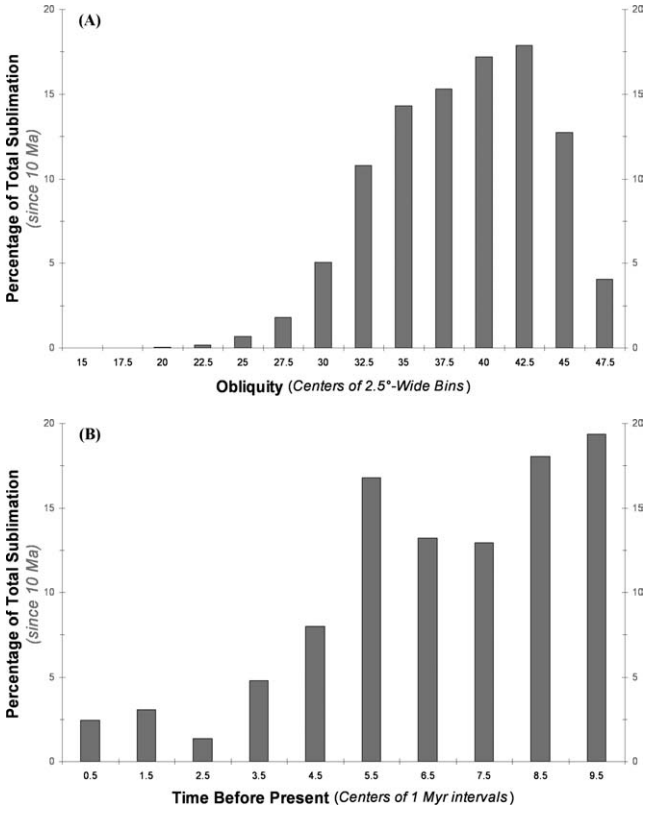

Fig. 13. North PLD sublimation history. (A) Integrated sublimation within 2.5°-wide obliquity bins, expressed as a fraction of the total sublimation over the last 10 Myr. (B) Integrated sublimation within each of the last ten Myr-intervals, expressed as a fraction of the total sublimation since 10 Ma. Both parts (A) and (B) assume the Fig. 2 martian obliquity history calculated by Touma and Wisdom (1993) and otherwise nominal North PLD conditions (Table 2).

2.5. Input parameter variations

Table 2 summarizes the effects of model input parameter variations upon predicted North PLD surface temperatures and sublimation rates. The first column lists all of the input parameters of our sublimation model, the nominal values of which are shown in the second column. Instead of the present-day $\theta = 25.2°$, we have adopted the median value of $\theta = 32.1°$ as the nominal obliquity for our parameter sensitivity study (since effects that only produce sublimation variations at lower obliquities will be largely irrelevant). The second row of Table 2 shows the "results for nominal conditions," which are an annual average surface temperature of $T_{sav} = 170$ K and a net annual sublimation rate of $E_{net} = 2.6$ pr. mm/yr. The third column lists the range of variations considered for each input parameter—the corresponding ranges of predicted T_{sav} and E_{net} (assuming nominal values for all other parameters) are shown in the fourth and fifth columns, respectively.

Table 2 reiterates the predominant influence that martian obliquity, which has varied from $\theta = 14°$ to $\theta = 48°$ over the last 10 Myr (Touma and Wisdom, 1993), has upon both North PLD surface temperatures and sublimation rates. In and of itself, raising eccentricity from the nominal $e = 0.0$ to the maximum value of $e = 0.1$ (Ward, 1992) has little effect upon net annual sublimation rates. However, coupling this increase with a change in perihelion passage to $\omega = 90°$ (i.e., perihelion at northern summer solstice) nearly doubles North PLD sublimation to $E_{net} = 5.6$ pr. mm/yr; conversely, the ($e = 0.1$, $\omega = 270°$) orbital configuration more than halves sublimation to $E_{net} = 1.2$ pr. mm/yr.

Table 2 indicates that variations in the surface properties of sublimating volatiles will also significantly impact T_{sav} and E_{net}, though not nearly as much as orbital fluctuations. Raising the albedo of water ice to $a = 0.5$ (the highest North PLD albedo measured by (Paige et al., 1994)) decreases T_{sav} by a few degrees and reduces E_{net} by about two-thirds, while lowering the albedo to our minimum $a = 0.3$ criterion for water ice (Section 2.2) slightly elevates T_{sav} and increases E_{net} by nearly 60%. Varying H_2O thermal inertia over the

Table 2
North PLD thermal and sublimation model input parameters

Parameter	Nominal	Range	Range of T_{sav} (K)	Range of E_{net} (mm/yr)
Results for nominal conditions			170	2.6
Obliquity (°)	32.1	14–48	148–181	0.0–19.3
Eccentricity	0.0	0.0–0.1	170–169	2.6–3.6
Argument of perihelion (°)	0	90–270 ($e = 0.1$)	168–172	5.9–1.2
Albedo	0.38	0.3–0.5	172–166	4.2–0.8
Thermal inertia (J/(m^2 s$^{1/2}$ K))	900	500–2000	168–173	2.9–1.6
Emissivity	1.0	0.9–1.0	172–170	4.3–2.6
Frost albedo	0.55	0.45–0.65	172–165	3.2–1.5
Frost emissivity	1.0	0.9–1.0	171–170	3.0–2.6
Diurnal advection efficiency	0.05	0–∞	170–169	0.0–23.4
Dust opacity	0.1	0.0–1.0	169–170	0.7–7.5
Atm. pressure (Pa)	700	350–1400	169–170	2.5–2.7
Wind speed (m/s)	10	1–20	170–170	2.5–2.5
Latitude (° N)	85	80–90	170–169	(Fig. 14A)
Surface slope (°) (+ = equatorward-facing)	0	(−10)–(+45)	(Fig. 19A)	(Fig. 15A)

List of nominal values as well as plausible ranges for each model input parameter, and effects of parameter variations upon annual average surface temperature and net annual sublimation rate for the North PLD.

500 J/(m^2 s$^{1/2}$ K) $< I_{th} <$ 2000 J/(m^2 s$^{1/2}$ K) range spanning most of the North PLD (Paige et al., 1994) produces relatively wide thermal variations, but has less of an effect (relative to changes in albedo) upon sublimation rates. Lowering surface water ice emissivity to the minimum value of $\varepsilon_s = 0.9$ considered by Haberle and Jakosky (1990) produces elevated surface temperatures and sublimation rates comparable to the case of $a = 0.3$, due to the similar effects of emissivity and albedo upon the surface heat balance (Eq. (2)). Relative to the analogous quantities for water ice, variations in CO_2 frost albedo or emissivity (Paige and Ingersoll, 1985) result in similar annually-averaged thermal swings but much smaller variations in H_2O sublimation.

Table 2 also indicates that variations in atmospheric input parameters, while having little impact on surface temperatures, can dramatically affect sublimation rates. As already shown in Fig. 13, raising the diurnal advection efficiency to $\varepsilon_{adv} = 0.5$ greatly reduces relative humidities, thereby increasing E_{net} fivefold to near the idealized ($r = 0$) limiting case of total instantaneous advection ($\varepsilon_{adv} = \infty$). Increasing atmospheric dust opacity to the estimated $\tau \sim 1$ optical depth of circumpolar dust storms (Cantor et al., 2001) also substantially augments E_{net} by reducing relative humidity, since the dust-induced warming of the atmosphere increases its water vapor holding capacity: by contrast, a colder dust-free $\tau = 0$ atmosphere inhibits surface sublimation. Variations in surface pressure (which may double at higher obliquities due to regolith desorption of CO_2: Fanale and Salvail, 1994) or near-surface wind-speed have little effect upon net annual sublimation rates for otherwise nominal conditions.

The two remaining input parameters are latitude, which ranges from 80° N to 90° N across the PLD, and surface slope, which varies from nearly 10° upon poleward-facing trough walls to more than 45° along steep equatorward-facing scarps (Section 1). The predicted ranges of net annual sublimation rate E_{net} resulting from these latitude and slope variations are not listed in Table 2, because each of these parameters affect sublimation via modification of surface insolation in a manner that varies with obliquity. Hence the obliquity sensitivity of the latitudinal and slope dependence of sublimation rate must be explicitly considered.

Figure 14A shows the latitudinal dependence of sublimation rate for a range of obliquities, normalized to the 85° N sublimation rate at each obliquity. For all four cases, total advection ($\varepsilon_{adv} = \infty$, $r = 0$) is assumed in order to maximize insolation-driven differences by minimizing atmospheric inhibition of sublimation (Fig. 12B). At the current obliquity of $\theta = 25.2°$ (long-dashed line), a nominal North PLD surface at 80° N experiences 33% more sublimation than an identical surface at 90° N. But for the median obliquity of $\theta = 32.1°$ (short-dashed line), the 80° N surface only experiences 5% more sublimation than a 90° N surface. The reason for this dampening is that at higher obliquities solar elevation angles increase throughout a martian day; consequently, the lower latitude benefit of receiving more insolation close to local noon is offset by the disadvantage of receiving less insolation during the now more illuminated "nighttime" hours. At $\theta = 37.5°$ (solid line), these opposing latitudinal effects effectively cancel each other out, as sublimation rates are essentially uniform from 80° N to 90° N. Indeed, by $\theta = 45°$ (dot-dashed line), the obliquity is so high that the 80° N surface actually experiences 2% *less* sublimation than a 90° N surface.

Figure 14B shows the recent 80° N and 90° N sublimation history for each of the last ten Myr-intervals, normalized to the total 85° N sublimation during each Myr-interval. Significant preferential sublimation of lower latitude North PLD surfaces is restricted to the last 3 Myr, when obliquities are generally below the median value of $\theta = 32.1°$ (Fig. 2). But because more than 80% of North PLD sublimation since 10 Ma takes place at higher obliquities (Fig. 13A), the long-term latitudinal dependence of North PLD sublimation rate

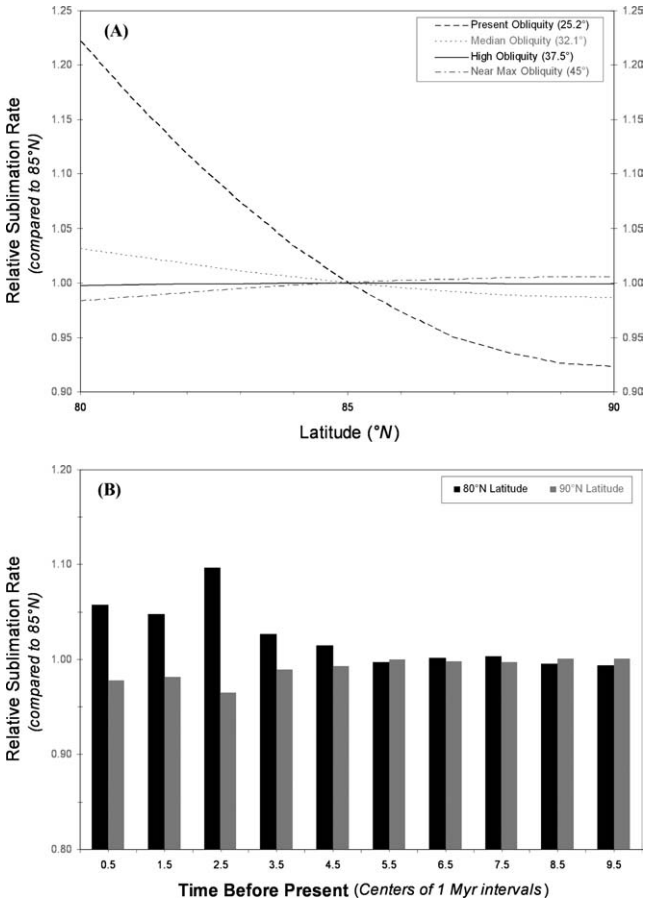

Fig. 14. Latitudinal dependence of North PLD sublimation. (A) Dependence of sublimation rate upon latitude, expressed relative to the net annual sublimation rate at 85° N, for four different obliquities and otherwise nominal North PLD conditions. (B) Integrated sublimation within each of the last ten Myr-intervals for surfaces at both 80° N and 90° N, expressed relative to the total sublimation since 10 Ma at 85° N, assuming the Touma and Wisdom (1993) martian obliquity history (Fig. 2) and otherwise nominal North PLD conditions (Table 2).

will be negligible. For example, our calculations indicate that the total sublimation from a 80° N surface, integrated over all of the last 10 Myr, exceeds that of an identical 90° N surface by less than 1%.

Therefore we conclude that the enhanced steepness of marginal scarps relative to interior troughs does not result from latitudinal variations in PLD sublimation. Furthermore, our modeling predicts that there should be no significant latitudinal variation of trough morphology, which is consistent with the observed lack of latitudinal dependence of either trough steepness (Fig. 7A) or trough depth (Fig. 7B).

2.6. Radiative trough balance

Surface slope is a crucial parameter within the context of evolutionary models of PLD morphology, which attribute the North PLD trough asymmetry ($\alpha_\varepsilon > \alpha_\rho$) to preferential sublimation of equatorward-facing trough walls (Howard et al., 1982; Clifford et al., 2000). The basic theory of sublimation-based North PLD trough modification generally involves three stages (Howard et al., 1982; Ivanov and Muhleman, 2000): (1) initial formation of a deep trough with symmetrical equatorward-facing and poleward-facing slopes due to a dust-related decrease in local ice albedo that increases sublimation rates (Table 2); (2) elimination of this local albedo contrast by eolian erosion; and (3) enhanced sublimation from equatorward-facing trough walls, which over time creates some sort of albedo-slope feedback that steepens equatorward-facing trough slopes.

We have three objections to this "standard" sublimation model of trough evolution. First, the exact details of the last step are somewhat vague—in particular, why enhanced sublimation of equatorward-facing trough walls should necessarily result in steeper equatorward-facing slopes, as opposed to simply increasing the rate of wall retreat from the center of the trough, is not clear. Second, a sublimation-based model requires that PLD troughs are initially characterized by a V-shape gentler than the mean poleward-facing trough wall slope of $\alpha_\varepsilon = -3.1°$ (so that subsequent sublimation can then steepen equatorward-facing trough walls to the current mean value of $\alpha_\varepsilon = 5.4°$). However, trough formation driven by a uniform surface albedo contrast should produce much steeper trough walls closer to the angle of repose. Thus an arbitrary non-uniform surface albedo contrast (maximized at the trough center and decreasing outward) is needed to produce suitably gentle initial trough slopes. Lastly, our most fundamental objection to evolutionary models involving preferential sublimation of equatorward-facing trough slopes is that, due to the effects of obliquity upon the slope dependence of sublimation from North PLD troughs, there actually is no long-term sublimation advantage of equatorward-facing trough walls.

Consider Fig. 15A, which shows the dependence of sublimation rate upon surface slope for four different obliquities, normalized to the untilted ($\alpha = 0$) sublimation rate at each obliquity. Total advection ($\varepsilon_{\text{adv}} = \infty$, $r = 0$) is again assumed in order to maximize insolation-driven differences in sublimation. At the current obliquity of $\theta = 25.2°$ (long-dashed line), a nominal North PLD surface with an equatorward-facing tilt of 10° ($\alpha_\varepsilon = 10°$) undergoes almost twice as much sublimation as an identical surface with a poleward-facing tilt of 10° ($\alpha_\varepsilon = -10°$). For our North PLD trough analysis, we define a "relative sublimation ratio" R_{EP} that measures the sublimation rates of surfaces corresponding to the mean equatorward-facing and poleward-facing trough wall slopes of $\alpha_\varepsilon = 5.4°$ and $\alpha_\varepsilon = -3.1°$, respectively; at the present obliquity, $R_{\text{EP}} = 1.33$.

However, the sublimation enhancement of equatorward-facing slopes is limited to lower obliquities (much like that associated with lower latitudes). For as obliquity increases and the average solar elevation rises, the benefit of being tilted towards the Sun close to local noon is offset by the disadvantage of being tilted away from the Sun during the now brighter nighttime hours. At the median obliquity of $\theta = 32.1°$ (short-dashed line), the relative sublimation ra-

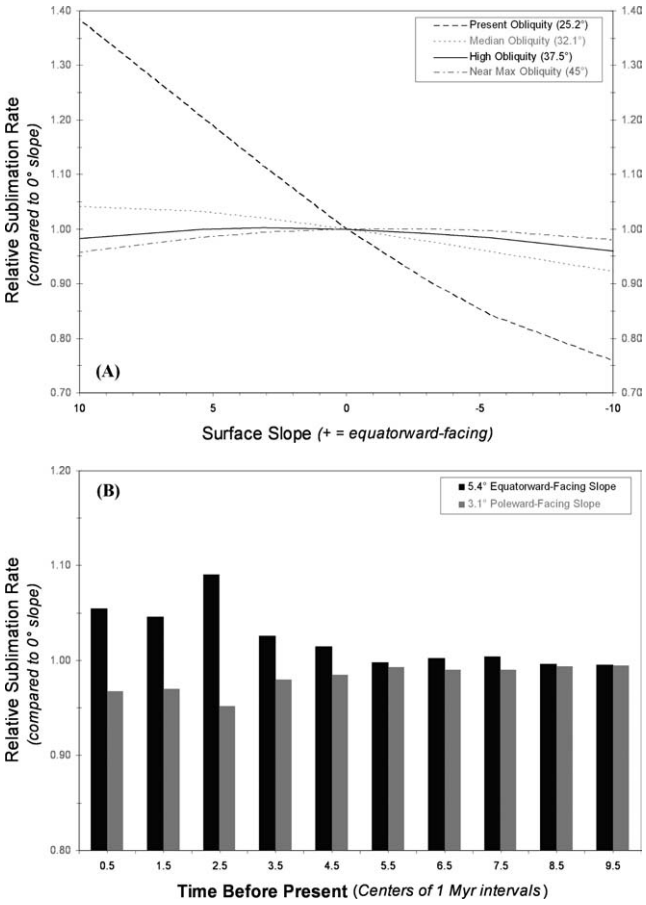

Fig. 15. Slope dependence of North PLD sublimation. (A) Dependence of sublimation upon equatorward-facing surface slope, expressed relative to the net annual sublimation rate at $\alpha_\varepsilon = 0°$, for four different obliquities and otherwise nominal North PLD conditions (Table 2). (B) Integrated sublimation within each of the last ten Myr-intervals for surfaces with equatorward-facing surface slopes of $\alpha_\varepsilon = +5.4°$ and $\alpha_\varepsilon = -3.1°$, expressed relative to the total sublimation from an untilted $\alpha_\varepsilon = 0°$ surface since 10 Ma, assuming the Touma and Wisdom (1993) martian obliquity history (Fig. 2) and otherwise nominal North PLD conditions (Table 2).

tio of opposing North PLD trough walls is just $R_{EP} = 1.06$. For $\theta = 37.5°$ (solid line), there is no longer any preferential sublimation of equatorward-facing trough walls, as R_{EP} falls to 1.00, and by $\theta = 45°$ (dot-dashed line), sublimation is actually slightly enhanced ($R_{EP} = 0.98$) from poleward-facing trough walls.

Figure 15B shows the recent $\alpha_\varepsilon = 5.4°$ and $\alpha_\varepsilon = -3.1°$ sublimation history for each of the last ten Myr-intervals, normalized to the untilted ($\alpha_\varepsilon = 0°$) sublimation during each Myr-interval. The long-term surface slope dependence of North PLD trough sublimation is nearly negligible, because equatorward-facing $\alpha_\varepsilon = 5.4°$ trough walls only experience a significant enhancement relative to poleward-facing $\alpha_\varepsilon = -3.1°$ trough walls at obliquities up to about $\theta \sim 35°$, and recall that more then two thirds of North PLD sublimation since 10 Ma takes place at higher obliquities (Fig. 13A).

Consequently, for the last 3 Myr of relatively low obliquity (Fig. 2), the relative equatorward-facing/poleward-facing sublimation ratio $R_{EP} = 1.10$, but over the entirety of the last 10 Myr, the relative sublimation ratio falls to slightly below $R_{EP} = 1.02$ (corresponding to an equatorward-facing/poleward-facing sublimation difference of less than 2%). Thus if present-day North PLD troughs formed at least 5–10 Ma, then neither equatorward-facing nor poleward-facing trough walls have experienced a significant long-term sublimation advantage due to variations in insolation. Although the asymmetry of North PLD troughs might still result from slope-dependent differential sublimation if trough modification has primarily occurred in the last few Myr, such a scenario is unlikely due to the much slower sublimation rates associated with low obliquities (Fig. 13A).

Therefore, counterintuitive as it may seem, we come to the conclusion that the steeper equatorward-facing slopes of North PLD trough walls probably do not result from insolation-driven preferential sublimation. But then what causes the asymmetry of opposing trough walls? Eolian erosion is of course one possible mechanism. In the next section, however, we suggest that viscous relaxation of subsurface water ice—which as shown in Pathare et al. (2005, this issue) is the modification mechanism most consistent with South PLD crater morphology—may also govern PLD trough and scarp evolution.

3. North PLD relaxation simulations

3.1. Limitations of the model

We have simulated the relaxation creep of North PLD troughs and scarps using Tekton, a finite element model developed by Melosh and Raefsky (1980) that we have also employed to study the viscous relaxation of craters within the South PLD (Pathare et al., 2005, this issue). Unfortunately, there are two fundamental reasons why North PLD troughs and scarps are far more difficult to model than South PLD craters. First, while the initial shape of craters can be reasonably estimated via comparison to fresh impact craters of similar diameter, no such relationship exists for troughs and scarps. For example, if a trough that is 400 m deep with average 4° slopes is undergoing relaxation, it could be a relatively young trough with initial depth of 500 m and initial 5° slopes, or it could be a much older trough that was originally significantly deeper and/or steeper. Second, unlike its dust-mantled southern counterpart, the icy surface of the North PLD is actively undergoing sublimation. Consequently, the surface mass balance is difficult to constrain within a 2D finite element model focused primarily upon "columnar" relaxation—indeed, a complete solution would require a three-dimensional glacial flow model that accounts for accumulation and ablation zones, which is beyond the scope of the present work.

Nevertheless, we feel that despite these limitations it is still instructive to present some idealized trough and scarp relaxation simulations, because of their implications for sev-

eral important issues related to North PLD morphology. These include: present-day and high obliquity trough closure times, the slope asymmetry of trough walls, and the slope–depth correlation of both troughs and scarps.

3.2. North PLD trough evolution

Although the 2D "planar" form of Tekton that we employ explicitly calculates both the normal and shear components of the stress deviator and strain rate tensors (Melosh and Raefsky, 1980), here it will be useful to focus upon the shear stress and strain rate computations. The gravitationally-induced driving stress τ_{xz} for an ice mass undergoing simple basal shear is given by (Nye, 1952):

$$\tau_{xz} = \rho g_z z \sin\alpha, \tag{3}$$

where ρ is the columnar density, g_z is the gravitational acceleration, z is the relative depth of the ice, and α is the effective surface slope, which is typically calculated over a lateral baseline of 10 times the depth (Paterson, 1994). The dependence of strain rate $\dot{\varepsilon}_{xz}$ upon the simple shear τ_{xz} can be explicitly expressed as (Durham and Stern, 2001):

$$\dot{\varepsilon}_{xz} = \hat{A}\tau_{xz}^n = f_s A \tau_{xz}^n \exp(-n b_d \phi_d) \exp(-Q/RT) d_i^{-p}, \tag{4}$$

where T is temperature, R is the gas constant, d_i is the diameter of the ice grain, ϕ_d is the volumetric fraction of dust in the ice, $b_d \sim 2$ is a dust-related flow constant (Durham et al., 1992), and n, A, Q, and p are laboratory-measured rheological parameters that relate the dependence of uniaxial compressive strain rate $\dot{\varepsilon}_i$ to uniaxial compressive stress σ_i (Nye et al., 2000)—which is a factor of $f_s = 3^{(n+1)/2}/2$ less than that of shear strain rate $\dot{\varepsilon}_{ij}$ to an equal magnitude shear stress τ_{ij} (Paterson, 1994).

At martian temperatures and pressures, the two water ice deformation mechanisms of greatest relevance are grain size sensitive (GSS) creep ($n = 1.8$, $A = 3.98 \times 10^{-3}$ MPa$^{-1.8}$ s^{-1}, $Q = 49$ kJ/mol, $p = 1.4$: Goldsby and Kohlstedt, 2001), and dislocation creep ($n = 4.0$, $A = 1.26 \times 10^5$ MPa^{-4} s^{-1}, $Q = 61$ kJ/mol, $p = 0$: Durham and Stern, 2001). Figure 16 shows the slope dependence of shear strain for both GSS and dislocation creep at typical PLD conditions, which as detailed in Pathare et al. (2005, this issue) can be characterized by: grain size $d_i = 1$ mm, dust fraction $\phi_d = 0.25$, density $\rho = 1500$ kg/m^3, heat flux $Q_g = 30$ mW/m^2, and thermal conductivity $K = 3$ W/(K m). Based upon our surface temperature calculations of Section 2.3, the present-day North PLD annual average surface temperature at 85° N is $T_{\text{sav}} = 162$ K (Fig. 12A). The steady state lapse rate can be expressed as $\Gamma = Q_g/K = 10$ K/km, corresponding to a subsurface temperature of $T = 172$ K at a depth of $z = 1$ km.

Figure 16 indicates that GSS and dislocation creep produce similar strain rates at moderately high α, but that the former dominates at lower effective surface slopes. Although Table 1 lists many North PLD troughs with surface slopes that approach $\alpha_\varepsilon = 10°$ along 1.6-km baselines,

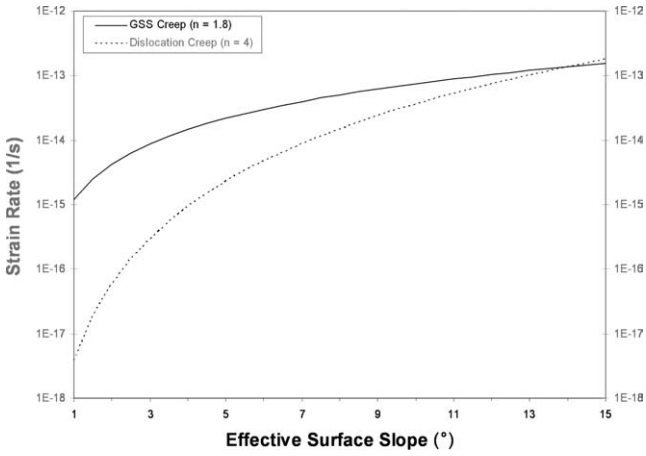

Fig. 16. Slope dependence of strain rate. Dependence of shear strain rate (Eq. (4)) upon effective surface slope for both GSS creep (Goldsby and Kohlstedt, 2001) and dislocation creep (Durham and Stern, 2001) of water ice at a depth of 1 km for "baseline" conditions (i.e., $d_i = 1$ mm; $\phi_d = 0.25$; $\Gamma = 10$ K/km) at the current annual average North PLD surface temperature of $T_{\text{sav}} = 162$ K.

Fig. 6E illustrates that over longer 10 km baselines (lowest line), the effective surface slopes "seen" at a depth of 1 km are consistently less than $\alpha = 5°$. Since the majority of deformation within a column occurs well below the surface (Paterson, 1994), we conclude that GSS creep is the predominant mechanism of North PLD trough relaxation, despite the relative steepness of the short-baseline surface slopes. Consequently, we have input the rheological parameters (n, A, Q, p) appropriate to GSS creep into our North PLD finite element simulations.

Figure 17 shows our planar Tekton simulations of North PLD trough relaxation for current thermal conditions. A 40 × 40 element grid is constructed that is 5 km deep and tens of km wide, with a vertical and horizontal grid point resolution that is maximized in the vicinity of the trough. According to Table 1, every North PLD trough identified along the Fig. 6 profiles has a total depth of less than $d = 1$ km, and all but one have maximum equatorward-facing wall slopes of below $\alpha_e = 10°$ (measured over a 1.6-km baseline). So for simplicity we will assume that all troughs form with an initial depth of $d_o = 1$ km and initial wall slopes of $\alpha_o = 10°$. Figure 17a shows the initial shape of the trough within a $Z = 2$ km thick layer of the North PLD (Table 1), in which the upper layer (darker shading) represents the deformable PLD while the lower layer (lighter shading) corresponds to immobile bedrock.

Predicted trough closure times for present-day North PLD thermal conditions are on the order of several million years. Although some deformation occurs during the first million years, by $t = 1$ Myr the trough has still not relaxed to half of its initial depth (Fig. 17b). Trough "closure"—which we define to occur at a relative depth of $d = 200$ m for consistency with our trough identification criterion (Table 1)—does not take place until almost $t = 5$ Myr (Fig. 17c). The PLD evolution illustrated in Fig. 17 differs markedly from

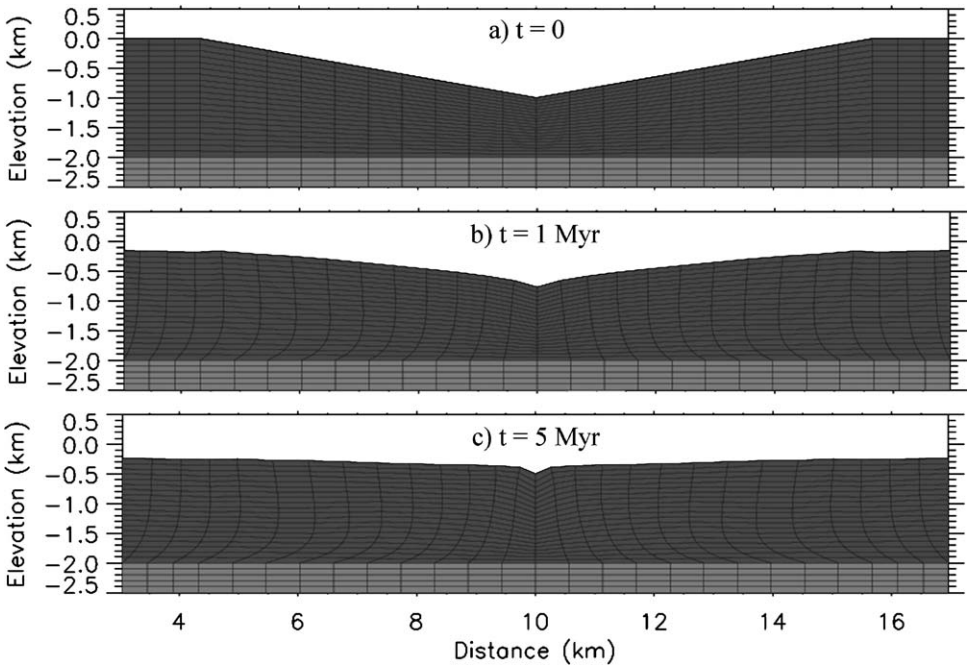

Fig. 17. North PLD trough relaxation (present-day thermal conditions). Relaxation history at time steps of $t = \{0, 1, 5\}$ Myr for baseline Tekton simulations of a North PLD trough with initial depth $d_o = 1$ km and initial wall slopes $\alpha_o = 10°$ at the present-day $T_{\text{sav}} = 162$ K. The deformable PLD layer is represented by the darker shading (which in this case has a thickness of $Z = 2$ km), in contrast to the immobile bedrock signified by the lighter-shaded layer.

that of terrestrial glaciers (Paterson, 1994), which quickly close large troughs on time scales of $t \ll 1$ Myr due to the higher stresses associated with steeper slopes (Eq. (3)). Indeed, based on the rapidity of terrestrial trough closure rates, Clifford et al. (2000) suggest that the continued presence of troughs in the martian PLD is inconsistent with widespread flow.

However, our Tekton simulations demonstrate the relatively slow rate of North PLD trough relaxation, which can be attributed to the colder North PLD temperatures and the lower stress dependence of GSS creep. As shown in Fig. 16, raising the effective surface slope from $\alpha = 1°$ to $5°$ produces a concomitant fivefold increase in shear stress τ_{xz} (Eq. (3)), which for $n = 4$ dislocation creep increases shear strain rates $\dot{\varepsilon}_{xz}$ by a factor of $5^4 = 620$, but for $n = 1.8$ GSS creep only increases shear strain rates by a factor of $5^{1.8} = 18$ (Eq. (4)). Since flow is dominated by GSS creep (Fig. 16), North PLD trough closure times are much longer than those associated with terrestrial glaciers, within which basal dislocation creep is more prominent (Paterson, 1994). Therefore, we conclude that the present ubiquity of troughs throughout the North PLD is not inconsistent with ongoing relaxation or flow.

North PLD trough closure is much more rapid at higher obliquities. Figure 18 plots the obliquity-dependent evolution of the total depth and maximum surface slope of North PLD troughs. For nominal steady-state thermal conditions ($\Gamma = 10$ K/km) at obliquities of $\theta = 25.2°$ ($T_{\text{sav}} = 161.8$ K) and $\theta = 35°$ ($T_{\text{sav}} = 172.1$ K), trough closure to a depth of below 200 m occurs at approximately $\tau_c = 4.5$ Myr and $\tau_c = 0.6$ Myr, respectively (Fig. 18A). Our high obliquity estimate is similar to the present-day calculations of Hvidberg (2003), who predicted North PLD trough closure times ranging from 0.1–1 Myr. However, Hvidberg (2003) assumed annual average surface temperatures at the North PLD margins as high as $T_{\text{sav}} = 175$ K, which is much warmer than the $T_{\text{sav}} = 162$ K that is most consistent with Viking IRTM observations (Paige et al., 1994); hence, we suggest that the rapid closure times of Hvidberg (2003) likewise apply to high obliquity conditions. Our results imply that present-day North PLD troughs cannot have formed much before the increase in mean martian obliquity that occurred $t \sim 4$ Ma (Fig. 2); otherwise, relaxation at the higher obliquities then prevalent would have quickly resulted in trough closure (thereby precluding current observation of said troughs).

North PLD troughs exhibit a strong correlation of maximum surface slope to total depth (Fig. 8). We suggest that the slope–depth correlation of North PLD troughs ($R_c = 0.78$) simply reflects the extremely similar relaxation histories predicted for total trough depth (Fig. 18A) and maximum surface slope (Fig. 18B). For example, Fig. 18C shows the current values of total trough depth and maximum surface slopes for nominal North PLD troughs ($\alpha_o = 10°$, $d_o = 1$ km, $Z = 2$ km) that form at times ranging from 0.5 Ma $< t <$ 4 Ma. (Note that for $\Gamma = 10$ K/km steady-state conditions, troughs older than $t = 4$ Ma would close due to a combination of high and present obliquity flow.) Since the ratio of total depth to maximum slope varies by less than 25%, the depths and slopes of North PLD troughs undergoing relaxation will be highly correlated, provided that initial formation conditions (i.e., α_o, d_o, Z) have been

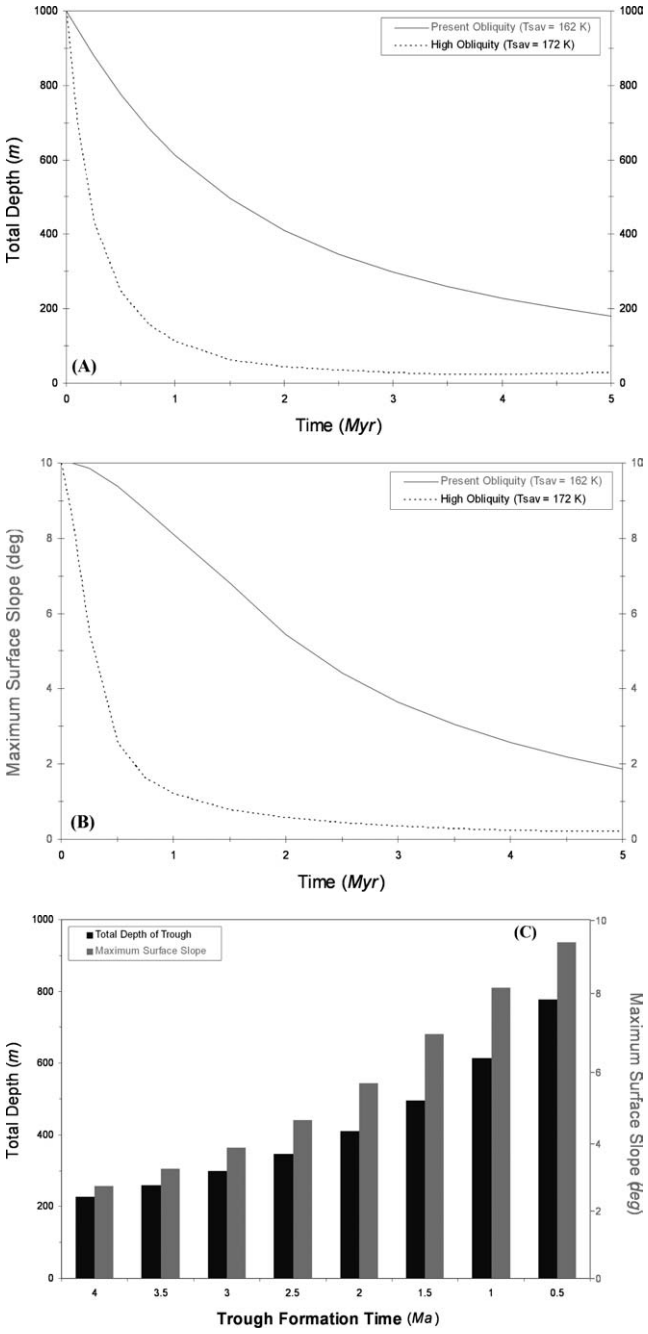

Fig. 18. North PLD trough evolution. (A) Temporal dependence of total crest-to-floor depth, derived from baseline North PLD trough simulations for both present-day ($T_{sav} = 162$ K) and high obliquity ($T_{sav} = 172$ K) thermal conditions. (B) Temporal dependence of maximum 1.6-km surface slopes, derived from baseline North PLD trough simulations for both present-day ($T_{sav} = 162$ K) and high obliquity ($T_{sav} = 172$ K) thermal conditions. (C) Side-by-side comparison of total crest-to-floor depths (left-hand bars) and maximum 1.6-km surface slopes (right-hand bars) corresponding to trough formation times spanning 0.5 Ma $< t <$ 4 Ma, derived from baseline North PLD trough simulations at present-day $T_{sav} = 162$ K.

broadly similar for most North PLD troughs. Thus viscous relaxation can provide a possible explanation for the correlation of trough depths and slopes.

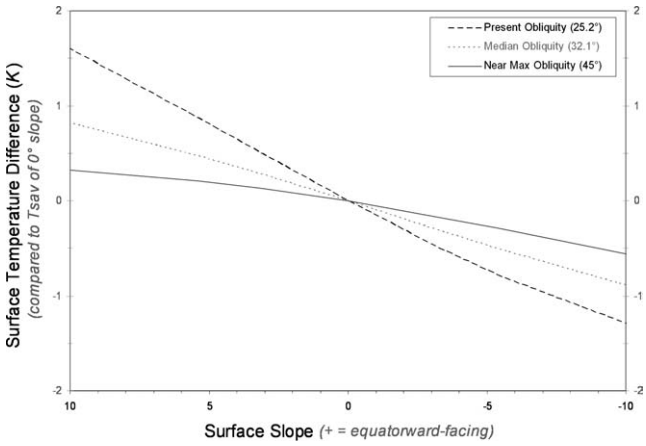

Fig. 19. Slope dependence of North PLD temperature. Dependence of annual average surface temperatures upon equatorward-facing surface slope, expressed relative to the T_{sav} at $\alpha_\varepsilon = 0°$, for three different obliquities and otherwise nominal North PLD conditions (Table 2).

But what about the slope asymmetry of North PLD troughs? We suggest that the enhanced steepness of equatorward-facing trough walls can be explained by intra-trough thermal variations, which can either result from the slope dependence of surface temperature or from albedo variations. For example, Fig. 19 shows the dependence of annual average surface temperature upon surface slope for three different obliquities, relative to the T_{sav} of an untilted ($\alpha = 0$) surface at each obliquity. At the present obliquity (long-dashed line), a nominal North PLD surface (Table 2) with an equatorward-facing tilt of $\alpha_\varepsilon = 5.4°$ (the mean value of maximum North PLD trough slope) is about 2 K warmer than an identical poleward-facing surface with $\alpha_\varepsilon = -5.4°$. (Note that the magnitude of the slope-induced thermal variation decreases at higher obliquities due to the increase in "nighttime" insolation.) For comparison, decreasing albedo from the nominal value of $a = 0.38$ to $a = 0.30$ also increases T_{sav} by 2 K (Table 1).

Figure 20 shows our planar Tekton simulations of North PLD trough relaxation for such differential thermal conditions. We assume that the equatorward-facing half of the trough ($x < 10$ km) is characterized by $T_{sav} = 161.8$ K, while the poleward-facing half ($x > 20$ km) is two degrees colder at $T_{sav} = 159.8$ K (a nominal lapse rate of $\Gamma = 10$ K/m is adopted for the entire trough). This slight thermal disparity is sufficient to produce a significant asymmetry in trough morphology by $t = 1$ Myr (Fig. 20b) that is even more pronounced at $t = 3$ Myr (Fig. 20c). Comparison of Fig. 20 to Fig. 17 (which assumed a uniform $T_{sav} = 161.8$ K) indicates that at $t = 1$ Myr the equatorward-facing trough walls in the two simulations are essentially identical. Hence, the asymmetry of Fig. 20 results from the slower rate of uplift of the inner poleward-facing trough walls, which can be attributed to the increased subsurface viscosity below the colder poleward-facing slopes.

Figure 21A plots surface profiles and slopes for each stage of the Fig. 20 North PLD trough simulations. The lag

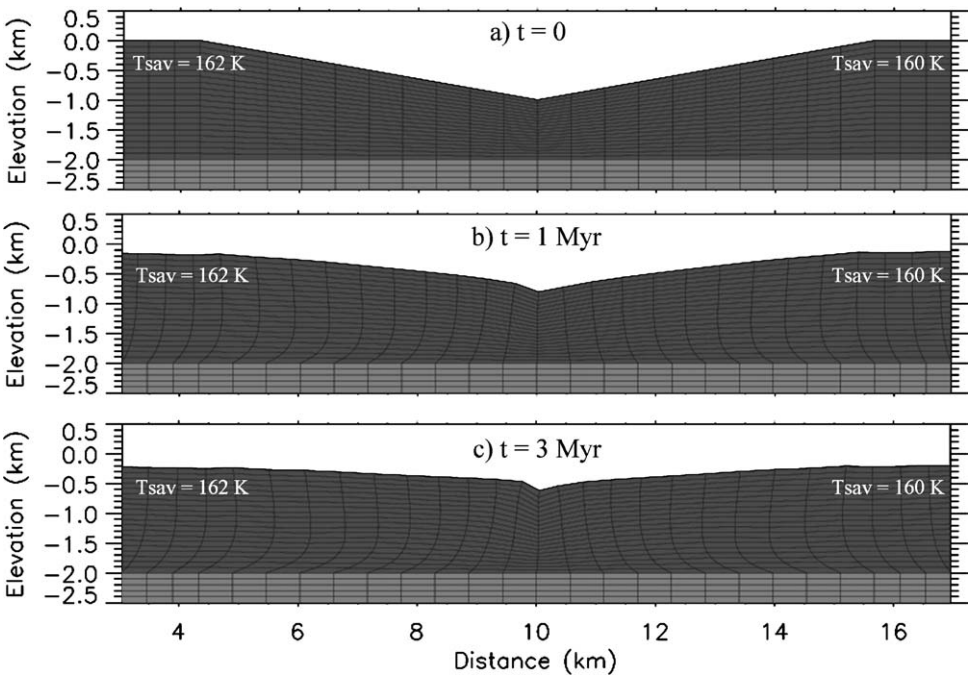

Fig. 20. North PLD trough relaxation (differential thermal conditions). Relaxation history at time steps of $t = \{0, 1, 5\}$ Myr for baseline simulations of a North PLD trough characterized by $T_{sav} = 162$ K upon the equatorward-facing wall and $T_{sav} = 160$ K upon the poleward-facing wall. A total PLD thickness of $Z = 2$ km is assumed.

in inner poleward-facing trough wall uplift leads to steeper equatorward-facing trough walls, as at $t = 1$ Myr the trough has maximum 1.6-km baseline slopes of $\alpha_\varepsilon = 10.1°$ and $\alpha_\rho = 9.2°$, and by $t = 3$ Myr the trough is characterized by $\alpha_\varepsilon = 6.7°$ and $\alpha_\rho = 5.3°$. Figure 21B compares the $t = 1$ Myr time step of the Tekton simulation (Fig. 20b) to actual gridded MOLA data of trough "A4" (Fig. 6A). The predicted and actual magnitudes of the surface slopes and relative depths are in good agreement, though the positioning of the predicted maximum equatorward-facing slope is much more central relative to the actual trough. This offset is likely due to enhanced sublimation from the equatorward-facing wall during the last few Myr of relatively low obliquities (Fig. 15B).

Of course, unlike trough evolution theories proposed by prior workers (e.g., Ivanov and Muhleman, 2000), within our model this preferential sublimation is not the root cause of the steepening of equatorward-facing surface slopes. For as shown in Fig. 22, by $t = 3$ Myr viscous relaxation produces an approximate ∼1.5° difference in maximum equatorward-facing and poleward-facing trough wall slopes, which is consistent with North PLD trough observations (Section 1.2). Consequently, we suggest that differential relaxation resulting from orbitally-modulated thermal fluctuations over the last few Myr—whether driven by insolation variations, albedo differences, or uneven CO_2 frost retention—can produce the slope asymmetry characteristic of most North PLD troughs.

3.3. PLD scarp evolution

The effects of orbitally-induced thermal variations are particularly important when considering the morphological evolution of PLD scarps. Figure 23a shows the initial shape of our nominal scarp simulations, which assume an initial slope of $\alpha_o = 5°$ and an initial depth (or equivalently, subcrest PLD thickness) of $d_o = 1$ km. For steady-state thermal conditions at the present obliquity ($T_{sav} = 161.8$ K, $\Gamma = 10$ K/km), the amount of relaxation over $t = 5$ Myr (Fig. 20b) is nearly negligible, due to the relative frigidity of the subsurface. However, for high obliquity thermal conditions ($\theta = 35°$, $T_{sav} = 172.1$ K), there is substantial deformation by $t = 5$ Myr (Fig. 23c), as in this scenario the warmer near-basal elements below the scarp crest experience significantly more strain (Eq. (4)), resulting in extensive lateral deformation that propagates into the colder scarp interior, ultimately leading to the compressive steepening of the scarp.

This means that long-term scarp steepness is governed almost entirely by high obliquity relaxation. Consequently, the evolution of scarp surface slopes over time spans longer than 10 Myr is effectively equivalent to the predicted steepening at high obliquity, divided by the fraction of time (f_θ) that martian obliquity can be classified as "high" (i.e., $\theta > 32.1°$). Although the precise obliquity history is uncertain prior to 10 Ma due to the chaotic nature of martian obliquity variations (Touma and Wisdom, 1993; Laskar et al., 2004), we will assume that long-term martian obliquity exceeds $\theta = 32.1°$ for on average $0.25 < f_\theta < 0.5$, which is

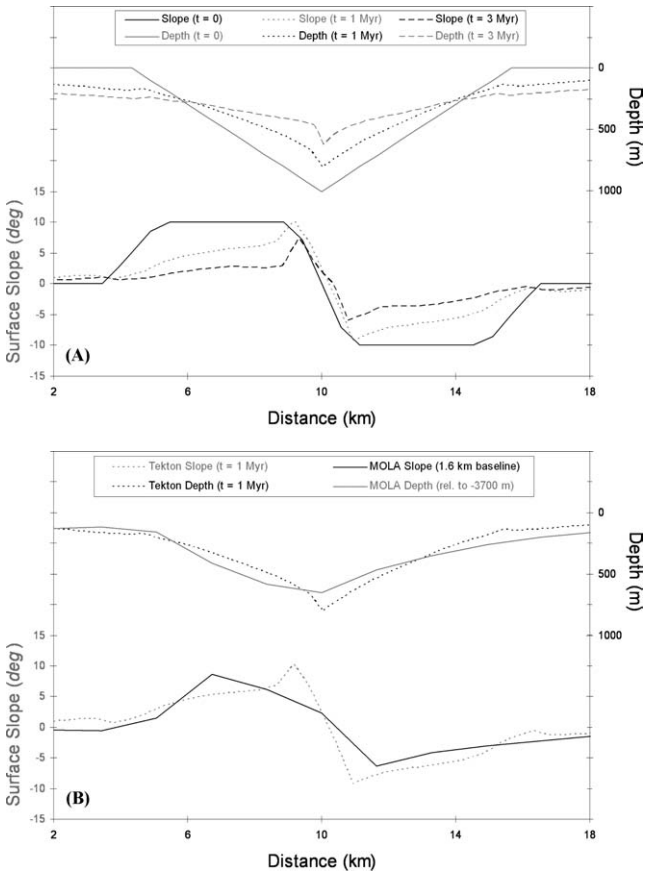

Fig. 21. North PLD trough evolution (differential thermal conditions). (A) Evolution of surface profile (upper lines) and 1.6-km surface slopes (lower lines) at time steps of $t = \{0, 1, 3\}$ Myr, derived from baseline North PLD trough simulations for differential thermal conditions characterized by $T_{\mathrm{sav}} = 162$ K upon the equatorward-facing wall and $T_{\mathrm{sav}} = 160$ K upon the poleward-facing wall (Fig. 20). (B) Comparison of predicted $t = 1$ Myr time step (dashed line) to actual relative depths and surface slopes derived from gridded MOLA data of trough "A4," the location of which is shown in Fig. 6A and Table 1.

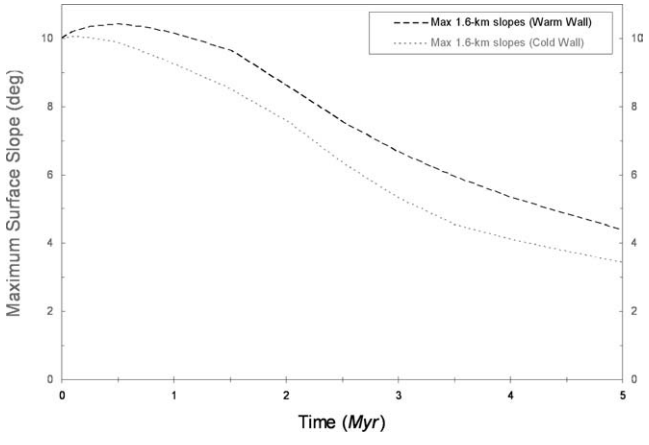

Fig. 22. North PLD trough slope evolution (differential thermal conditions). Evolution of maximum 1.6-km surface slopes for both equatorward-facing and poleward-facing trough walls, derived from baseline North PLD trough simulations for differential thermal conditions characterized by $T_{\mathrm{sav}} = 162$ K upon the equatorward-facing wall and $T_{\mathrm{sav}} = 160$ K upon the poleward-facing wall (Fig. 20).

consistent with the $f_\theta = 0.41$ that characterizes the sample 100 Myr obliquity history calculated by Touma and Wisdom (1993). Thus our long-term simulations of the evolution of scarp relaxation shown in Fig. 24 (for $d_o = 1$ km and $\alpha_o = 5°$) indicate that after $t = 25/f_\theta = 50$–100 Myr, maximum scarp slopes will increase to $\alpha_\varepsilon = 12.3°$, which is in good agreement with the $9° < \alpha_\varepsilon < 15°$ range of slopes observed for the four North PLD primary scarps that are approximately 1 km deep (Fig. 8; Table 1).

Figure 25 shows the sensitivity of our finite-element simulations to the initial depth of the scarp. For $d_o = \{0.5, 1.0, 1.5\}$ km, the maximum surface slope after 10 Myr of high obliquity thermal conditions ($T_{\mathrm{sav}} = 172.1$ K, $\Gamma = 10$ K/km) is $\alpha_\varepsilon = \{5.7°, 8.5°, 15.8°\}$. Hence our relaxation modeling predicts that shallow scarps ($d < 500$ m) will not experience significant slope augmentation, whereas walls along deeper scarps will undergo considerable steepening. The depth dependence of scarp morphology provides an excellent explanation for the strong correlation between maximum scarp slope and total scarp depth observed within the North PLD (Fig. 8). This effect also explains why primary scarps, which have an average depth of 1 km, are generally so much steeper (mean $\alpha_\varepsilon = 13.0°$) than secondary scarps (mean $\alpha_\varepsilon = 5.6°$), which have a shallower average depth of 500 m (Table 1; Fig. 8).

The slope dichotomy of primary and secondary scarps is particularly problematic for non-relaxation evolutionary models, for if sublimation or eolian erosion is the main cause of primary scarp steepening, then why are nearby secondary scarps—which presumably share a similar surface ablation history due to their proximity—not also steep? Since subsurface relaxation can also explain the correlation of NPLD trough slopes with depth (Fig. 18C), we conclude that viscous relaxation is consistent with many of the key topographic observations of North PLD trough and scarp morphology.

4. Discussion

4.1. PLD trough evolution

The results of both our sublimation modeling (Section 2) and relaxation simulations (Section 3) indicate that North PLD troughs are relatively young features. For if North PLD troughs predate the last high obliquity epoch (5 Ma $< t <$ 10 Ma), then neither equatorward-facing nor poleward-facing walls experience a significant long-term sublimation advantage (Fig. 15B), which means that the observed trough slope asymmetry cannot be sustained by preferential sublimation of equatorward-facing walls. Moreover, trough closure relaxation times (to a depth of less than $d = 200$ m) at high obliquities are much shorter than at present (Fig. 18A), due to increased subsurface temperatures. Therefore, we conclude that most North PLD troughs have probably formed within the last 5 Myr.

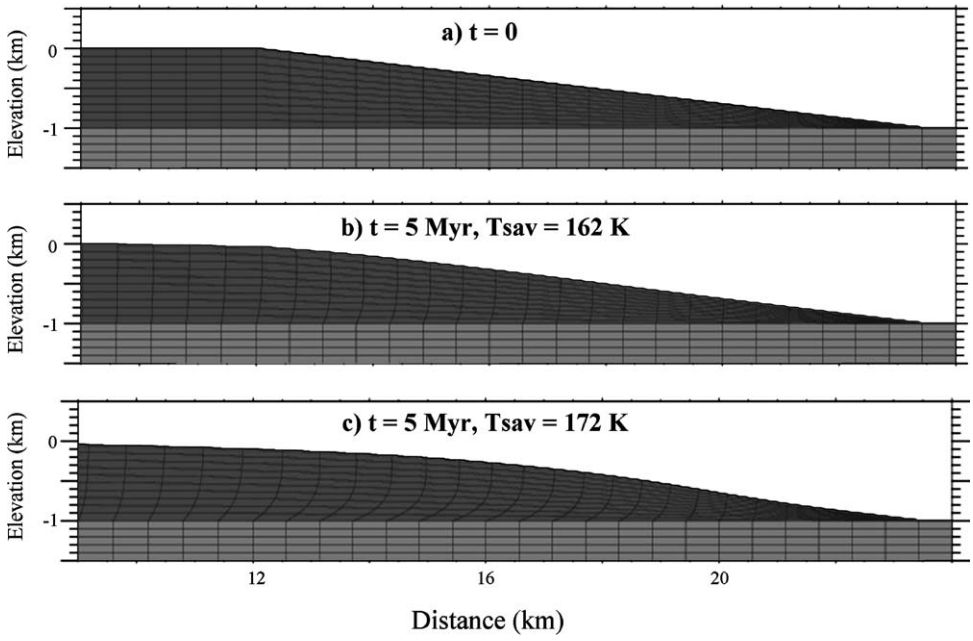

Fig. 23. North PLD scarp relaxation (steady-state thermal conditions). Relaxation history at time steps of $t = \{0, 5\}$ Myr for baseline Tekton simulations of a North PLD scarp with (a) initial sub-crest thickness $Z = 1$ km and initial wall slope $\alpha_o = 5°$, for both (b) present-day $T_{sav} = 162$ K and (c) $T_{sav} = 172$ K characteristic of higher obliquities.

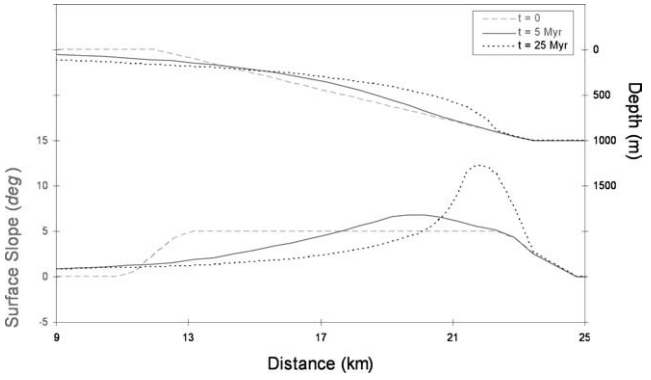

Fig. 24. North PLD scarp evolution (high obliquity thermal conditions). High obliquity evolution of surface profile (upper lines) and 1.6-km surface slopes (lower lines) at time steps of $t = \{0, 5, 25\}$ Myr, derived from baseline North PLD scarp simulations for $T_{sav} = 172$ K (Figs. 23a, 23c).

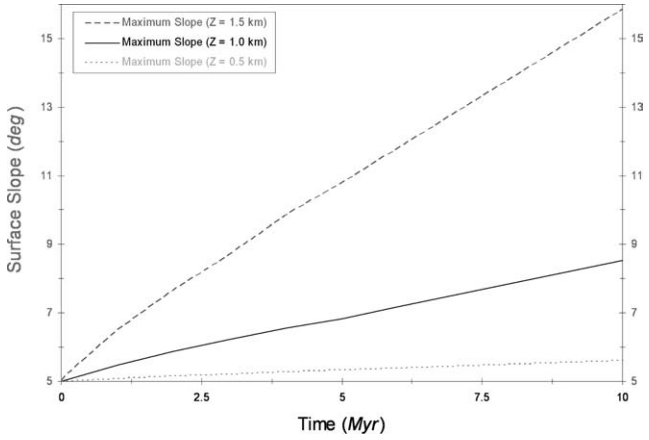

Fig. 25. Depth dependence of scarp evolution (high obliquity thermal conditions). Evolution of maximum 1.6-km surface slopes derived from baseline North PLD scarp simulations (Fig. 23) for PLD thicknesses of $Z = \{1.5, 1.0, 0.5\}$ km and typical high obliquity value of $T_{sav} = 172$ K.

The formation times of North PLD troughs can be further constrained by even more recent obliquity variations. We assume that trough formation results from a dust-related decrease in local ice albedo that increases sublimation rates (Howard et al., 1982; Ivanov and Muhleman, 2000), producing a symmetric trench at the site of the albedo contrast. For example, consider a trough formation scenario involving local accumulation of dusty low-albedo water ice with $a = 0.30$. For typical low obliquity, low advection North PLD conditions ($\theta = 25.2°$, $\varepsilon_{adv} = 0.05$), the sublimation rate from an $a = 0.30$ surface is 0.38 pr. mm/yr greater than that of an analogous nominal albedo ($a = 0.38$) surface. Hence the time required to sublimate down to the mean North PLD relative trough depth of 440 m (Table 1) is $t_{sub} = 440$ m/(0.00038 m/yr) = 1.2 Myr. But for typical moderate obliquity, moderate advection conditions ($\theta = 35°$, $\varepsilon_{adv} = 0.50$), the sublimation rate from an $a = 0.30$ surface is 16 pr. mm/yr greater than that of a comparable $a = 0.38$ surface, resulting in a faster trough sublimation time of $t_{sub} = 440$ m/(0.016 m/yr) = 27 kyr.

Since the long-term persistence of surface albedo contrasts is potentially limited by eolian redistribution, trough formation is clearly favored at higher obliquities. But whereas martian obliquity has been greater than $\theta = 35°$ for less than 1% of the last 3 Myr, it exceeded $\theta = 35°$ for more than 20% of the interval ranging from 5 Ma $< t <$ 3 Ma (Fig. 2). Consequently, widespread ongoing formation of North PLD troughs is highly unlikely; instead, most extant

North PLD troughs probably formed during the transitional period from high to low mean obliquity that martian orbit models consistently place at $t \sim 4$ Ma (Ward and Rudy, 1991; Touma and Wisdom, 1993).

The central morphological question considered here is: what mechanism has governed the subsequent evolution of North PLD troughs? More specifically, does the North PLD trough asymmetry somehow result from preferential sublimation of equatorward-facing walls during the last few Myr (Fig. 15B)—despite the greatly reduced sublimation rates at lower obliquities (Fig. 13A)? Perhaps eolian erosion has unevenly modified opposing trough walls? Or is the slope asymmetry produced by differential relaxation of equatorward-facing and poleward-facing trough walls that arises from insolation-driven thermal variations (Fig. 22)? The strong correlation of trough depth and slope (Fig. 8), which is difficult to explain in terms of sublimation or eolian erosion, is consistent with the predicted relaxation history of North PLD troughs (Fig. 18C).

Additional support for the relaxation hypothesis is provided by the observed stratigraphy of North PLD troughs. Figure 26A shows a high-resolution MOC observation of a typical North PLD trough (the location of which is outlined in the wide-angle context image of Fig. 26B). Howard et al. (1982) divided PLD troughs into three main stratigraphic units: (1) Layered Terrain, expressed upon equatorward-facing trough slopes; (2) Banded Terrain, located on poleward-facing trough walls; and (3) Smooth Terrain, which spans the regions between the troughs.

The equatorward-facing Layered Terrain are comprised of clearly delineated fine-scale laminae (Fig. 1), most of which are relatively dark in appearance. The continued visibility of these layers implies active resurfacing by not only water ice sublimation but also eolian erosion—otherwise, a sublimation dust lag would be expected to form (Hofstadter and Murray, 1990; Howard, 2000). The wider layers of the intermediate-toned poleward-facing Banded Terrain are much more irregular, and have been interpreted by Howard et al. (1982) as representing the eroded "feather edges" of ice or dust layers deposited on poleward-facing trough walls. These two stratigraphic units provide the basis for the standard model of trough evolution in which water ice sublimated from the equatorward-facing Layered Terrain recondenses upon the poleward-facing Banded Terrain, resulting in the poleward migration of the trough (Howard, 1978; Toon et al., 1980; Howard et al., 1982).

However, we argue that the relative thinness of the Banded Terrain actually indicates that deposition within troughs is insignificant. The diffuse Banded Terrain often appear to be translucent (e.g., Fig. 13 of Howard et al., 1982), exposing underlying fine-scale layers upon poleward-facing trough walls that are continuous with their equatorward-facing Layered Terrain counterparts. But according to the calculations of Bass et al. (2000), deposition of a millimeter-thick layer is more than sufficient to alter surface albedo and obscure the trough wall. If we conservatively assume that the average thickness of the Banded Terrain is a full meter, then given that most present-day North PLD troughs likely formed about 4 Ma, the implied net deposition rate is only 0.25 microns per year—or about three orders of magnitude less than the North PLD sublimation rate of 0.19 mm/yr derived from Viking MAWD data (Section 2.2).

The bright Smooth Terrain, which corresponds to the water ice surface of the North Permanent Cap (NPC), gradually transitions into the Layered Terrain (Fig. 26A), which is why the NPC is widely presumed to simply represent the uppermost layer of the North PLD (Clifford et al., 2000). Although the Smooth Terrain often appears to be featureless in summertime images (e.g., Fig. 26B), springtime observations such as Fig. 26C that highlight topography (due to the ubiquity of the seasonal CO_2 frost cap) reveal the presence of gentle wave-like undulations (Cutts et al., 1979). These shallow undulations typically have a vertical amplitude of 10–100 m, and are most prominent parallel to the equatorward (i.e., southern) edge of North PLD troughs (Howard, 2000). In the context of trough migration, Squyres (1979) suggested that the undulations are "scars" representing the former positions of trough floors undergoing poleward retreat. As noted by Howard (2000), the main difficulty with this theory is that the troughs are currently substantially deeper than the undulations; hence, some mechanism must have increased the depth of the troughs while preserving the shallowness of the undulations, which considering their proximity seems unlikely.

The other alternative is that the undulations were formerly much deeper and have subsequently experienced massive infill. But the rate of trough deposition implied by the thin poleward-facing Banded Terrain layers is much too low to raise deep trough floors by several hundred meters on Myr time scales. However, our finite element simulations of North PLD troughs (Section 2.4) demonstrate that viscous relaxation can produce such rapid trough floor uplift, particularly at high obliquities (Fig. 18A). Furthermore, our modeling indicates that troughs that have attained "closure" (defined for convenience as the time when $d < 200$ m) still retain a distinct V-shape (e.g., Fig. 17c) which is similar in appearance to the gentle trough-like morphology of undulations (Howard, 2000).

Therefore, we propose that undulations within the Smooth Terrain represent relict paleo-troughs that have experienced closure via viscous relaxation. Similarly, the slope asymmetry of present-day North PLD troughs is concordant with differential flow rates resulting from intra-trough thermal variations (Fig. 22), which could either result from the expected slope dependence of surface temperature (Fig. 19A) or from the generally lower albedo of equatorward-facing Layered Terrain relative to poleward-facing Banded Terrain (Fig. 26A). Thus we suggest that viscous relaxation is the modification mechanism most consistent with both the stratigraphy and topography of troughs within the North Polar Layered Deposits.

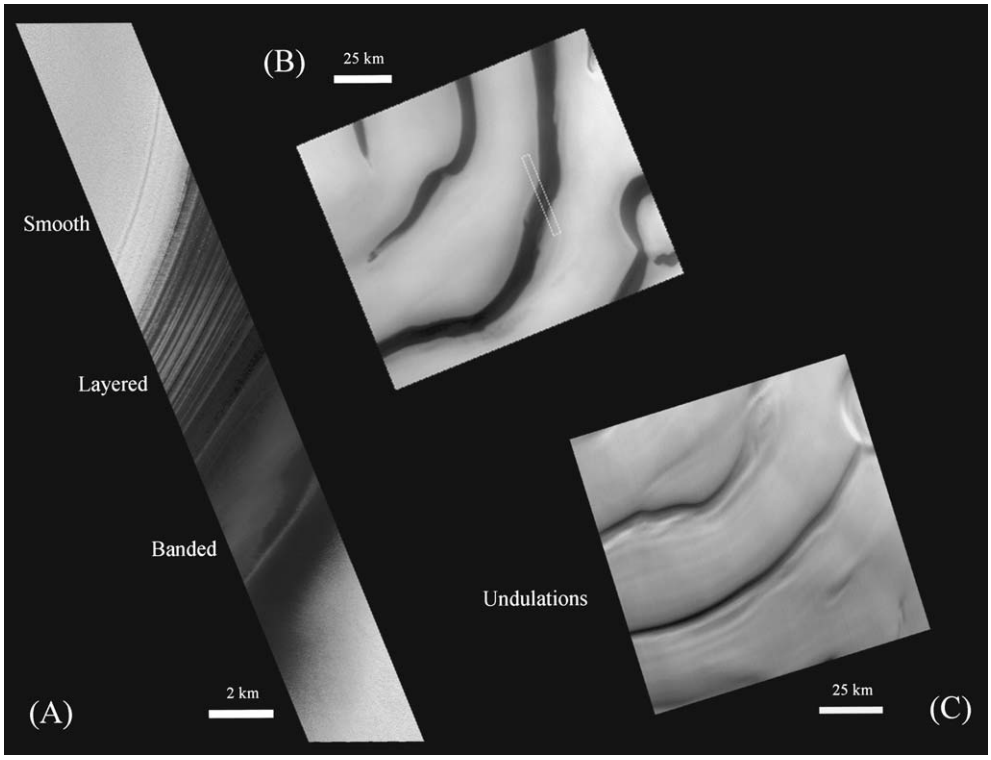

Fig. 26. North PLD trough stratigraphy. Three MOC images plotted in polar stereographic projection: (A) E01-01092: 87.0° N, 264.4° W, resolution = 13.0 m/pixel, size = 3.34 × 36.3 km, $L_s = 118°$; (B) E01-01093: 87.4° N, 265.8° W, resolution = 274 m/pixel, size = 133 × 113 km, $L_s = 118°$; (C) (M18-00805) 86.7° N, 282.4° W, resolution = 272 m/pixel, size = 133 × 114 km, $L_s = 35°$. Context for part (A) shown in part (B). North is towards the top of all three images: (A) and (B) are illuminated from the left, (C) from above. Layered terrain in (A) lies on equatorward-facing slopes, opposed by poleward-facing banded terrain.

4.2. *Recent evolution of the North PLD*

Although our modeling suggests that both interior troughs and marginal scarps within the North PLD undergo relaxation, they do so over significantly different time scales. As shown in Section 3.3, our long-term simulations of scarp relaxation (for an initial slope of $\alpha_o = 5°$) predict that approximately 50–100 Myr are required to steepen maximum surface slopes to the $\alpha_\varepsilon \sim 10°$ range presently observed for $d \sim 1$ km primary North PLD scarps (Fig. 8; Table 1). Interestingly, such stability at the margins of the North PLD is broadly consistent with the greater than 100 Myr surface ages implied by retention of large $D > 6$ km craters located at the periphery of the North PLD (Pathare et al., 2005, this issue).

In contrast, trough closure considerations dictate that present-day North PLD troughs have probably formed within the last 5 Myr (Fig. 18A). However, even this relatively young formation time is an order of magnitude greater than the maximum surface ages of approximately 300 kyr derived from the lack of mid-sized craters (0.5 km < D < 5 km) throughout the interior of the North PLD (Herkenhoff and Plaut, 2000; Pathare et al., 2005, this issue). Moreover, viscous relaxation cannot explain the absence of such craters upon the inter-trough Smooth Terrain (Fig. 26A), since the calculations of Pathare et al. (2005, this issue) indicate that eradication of mid-sized craters occurs on 100 Myr time scales.

Consequently, some other resurfacing mechanism must be responsible for the extraordinary youthfulness of trough-related stratigraphic units within the North PLD. Given the widespread presence of water ice at the surface of the North PLD (Paige et al., 1994), the most likely processes are H_2O sublimation and/or condensation (Section 1.2). Almost all models of recent PLD evolution presume that the equatorward-facing Layered Terrain (Fig. 26A) is actively sublimating, since its unobscured fine-scale layering clearly indicates a lack of present-day accumulation (Howard et al., 1982), and because the slope dependence of sublimation favors equatorward-facing trough walls at the current obliquity (Fig. 15A). However, the relative importance of sublimation and condensation upon other units is more contentious.

The uniformitarian hypothesis advanced by Howard (1978) assumes that water ice sublimated from equatorward-facing Layered Terrain continually condenses upon both opposing poleward-facing Banded Terrain and adjacent flat-lying Smooth Terrain, a pattern that results in the steady poleward migration of the trough (Howard et al., 1982). The evidence for deposition upon the Banded Terrain mainly consists of that unit's characteristically wide and diffuse layers (Howard et al., 1982)—although as discussed in Section 4.1, the magnitude of such deposition is limited by the

apparent thinness of these bands. As for the Smooth Terrain, Fisher (2000) argues by way of analogy with terrestrial glaciers that the bright whitish hue of this unit is indicative of accumulation, in contrast to the ablation implied by the darker Layered Terrain.

However, this simple albedo-based argument is stratigraphically inconsistent. For even though the poleward-facing Banded Terrain is more favored for condensation than the flat-lying Smooth Terrain (which according to Fig. 15A presently undergoes more sublimation than a poleward-facing slope), the Banded Terrain generally has an albedo intermediate between that of the dark Layered Terrain and the bright Smooth Terrain (Fig. 26A). In other words, if the Smooth Terrain has a high albedo because it is accumulating fresh water ice, then why is the Banded Terrain not at least as bright?

Therefore, we argue that the inter-trough Smooth Terrain is undergoing net sublimation, along with the equatorward-facing Layered Terrain. Moreover, the obliquity dependence of sublimation (Fig. 12A) suggests that the poleward-facing Banded Terrain may also be ablating. For example, our sublimation modeling predicts that the $\theta = 26.2°$ summertime sublimation rate from a nominal $\alpha_\varepsilon = -3.1°$ North PLD surface (corresponding to the mean slope of poleward-facing trough walls) is $E_{\text{net}} = 0.43$ mm/yr, which is slightly *greater* than the present obliquity ($\theta = 25.2°$) $E_{\text{net}} = 0.42$ mm/yr calculated for a nominal $\alpha_\varepsilon = 5.4°$ North PLD surface (characteristic of the mean slope of equatorward-facing trough walls). These results imply that opposing trough walls are in different sublimation/condensation regimes for a relatively narrow obliquity window (the actual width of which depends upon the uncertain orbital modulation of wintertime H_2O recondensation). Hence we suspect that the diffuse bands observed upon poleward-facing trough walls result from deposition at lower obliquities, and that over the probable 3–5 Myr lifetimes of North PLD troughs (Section 2.4), the poleward-facing Banded Terrain undergoes net sublimation.

Consequently, we suggest that long-term deposition of H_2O does not occur anywhere in the vicinity of troughs. Instead, we propose that net condensation of water ice is restricted to the very center of the North PLD—where as seen in Figs. 3 and 4 troughs are absent—via the "vacuum effect" associated with repeated H_2O recondensation within the retreating seasonal CO_2 cap (Section 1.2), as predicted by GCM modeling (Houben et al., 1997) and corroborated by Viking observations (Bass and Paige, 2000). However, this scenario of widespread ablation throughout the outer North PLD and focused accumulation within the inner North PLD raises long-term stability concerns, since the MAWD-derived average North PLD sublimation rate of $E_{\text{net}} = 0.19$ mm/yr (Section 1.2) is fast enough to transfer a $Z = 1$ km thick layer from the outer to the inner North PLD in a little over 5 Myr. Thus in order to prevent massive thickening near the pole, some process must be redistributing material back to the margins.

Our modeling suggests that glacial flow may be the most likely mechanism of maintaining mass balance within the North PLD. For not only do our sublimation calculations indicate that the North PLD is divided into ablation and accumulation zones (much like terrestrial glaciers), but our finite element relaxation simulations suggest that the PLD consist of deformable ice—which is a fundamental prerequisite for glacial flow. Furthermore, the flow modeling of Budd et al. (1986) and Nye (2000) shows that the domal topography of the North PLD is consistent with glacial spreading. Therefore, flow processes may not only control the relaxation history of mid-sized features such as troughs and scarps, but may also govern the large-scale morphological evolution of the entire North Polar Layered Deposits.

Acknowledgments

The authors thank the MOLA Science Team for releasing extremely useful topographic data grids and analysis tools to the scientific community. The authors also acknowledge the use of Mars Orbiter Camera images processed by Malin Space Science Systems that are available at http://www.msss.com/moc_gallery. This work was supported by NASA Grants NNG04GJ826 and NAG5-10973. Last, the authors thank Kathryn Fishbaugh and an anonymous reviewer for the breadth and depth of their comments and suggestions.

References

Bass, D.S., Paige, D.A., 2000. Variability of Mars' north polar water ice cap. II. Analysis of Viking IRTM and MAWD data. Icarus 144, 397–409.

Bass, D.S., Herkenhoff, K.E., Paige, D.A., 2000. Variability of Mars' north polar water ice cap. I. Analysis of Mariner 9 and Viking Orbiter imaging data. Icarus 144, 382–396.

Budd, W.F., Jenssen, D., Leach, J.H.I., Smith, I.N., Radok, U., 1986. The north polar ice cap of Mars as a steady state system. Polarforschung 56, 43–63.

Cantor, B.A., James, P.B., Caplinger, M., Wolff, M.J., 2001. Martian dust storms: 1999 Mars Orbiter Camera observations. J. Geophys. Res. 106 (E10), 23653–23688.

Clifford, S., 52 colleagues, 2000. The state and future of Mars polar science and exploration. Icarus 144, 210–242.

Cutts, J.A., Lewis, B.H., 1982. Models of climate cycles recorded in martian polar layered deposits. Icarus 50, 216–244.

Cutts, J.A., Blasius, K.R., Roberts, W., 1979. Evolution of martian polar landscapes. Interplay of long-term variations in perennial ice cover and dust storm intensity. J. Geophys. Res. 84, 2975–2994.

Durham, W.B., Stern, L.A., 2001. Rheological properties of water ice—applications to satellites of the outer planets. Annu. Rev. Earth Planet. Sci. 29, 295–330.

Durham, W.B., Kirby, S.H., Stern, L.A., 1992. Effects of dispersed particulates on the rheology of water ice at planetary conditions. J. Geophys. Res. 97, 20883–20897.

Fanale, F.P., Salvail, J.R., 1994. Quasi-periodic atmosphere-regolith-cap CO_2 redistribution in the martian past. Icarus 111, 305–316.

Fishbaugh, K.E., Head III, J.W., 2000. North polar region of Mars: topography of circumpolar deposits from Mars Orbiter Laser Altimeter (MOLA) data and evidence for asymmetric retreat of the polar cap. J. Geophys. Res. 105, 22455–22486.

Fisher, D.A., 2000. Internal layers in an "accublation" ice cap: a test for flow. Icarus 144, 289–294.

Goldsby, D.L., Kohlstedt, D.L., 2001. Superplastic deformation of ice. Experimental observations. J. Geophys. Res. 106, 11031–11042.

Haberle, R.M., Jakosky, B.M., 1990. Sublimation and transport of water from the north residual polar cap of Mars. J. Geophys. Res. 95, 1423–1437.

Herkenhoff, K., Plaut, J., 2000. Surface ages and resurfacing rates of the polar layered deposits on Mars. Icarus 144, 243–255.

Hofstadter, M.D., Murray, B.C., 1990. Ice sublimation and rheology: implications for the martian polar layered deposits. Icarus 84, 352–361.

Houben, H., Haberle, R.M., Young, R.E., Zent, A.P., 1997. Modeling the martian seasonal water cycle. J. Geophys. Res. 102, 9069–9083.

Howard, A.D., 1978. Origin of the stepped topography of the martian poles. Icarus 34, 581–599.

Howard, A.D., 2000. The role of eolian processes in forming surface features of the martian polar layered deposits. Icarus 144, 267–288.

Howard, A.D., Cutts, J.A., Blasius, K.R., 1982. Stratigraphic relationships within martian polar cap deposits. Icarus 50, 161–215.

Hvidberg, C.S., 2003. Relationship between topography and flow in the north polar cap of Mars. Ann. Glaciol. 37, 363–369.

Imbrie, J., 1982. Astronomical theory of the Pleistocene ice ages: a brief historical review. Icarus 50, 408–422.

Ingersoll, A.P., 1970. Mars: occurrence of liquid water. Science 168, 972–973.

Ivanov, A.B., Muhleman, D.O., 2000. Comparative analysis of the martian ice caps topography: results from the Mars Orbiter Laser Altimeter (MOLA) investigation. Icarus 144, 436–448.

Jakosky, B.M., Carr, M.H., 1985. Possible precipitation of ice at low latitudes of Mars during periods of high obliquity. Nature 315, 559–561.

Jakosky, B.M., Farmer, C.B., 1982. The seasonal and global behavior of water vapor in the Mars atmosphere: complete global results of the Viking atmospheric water detector experiment. J. Geophys. Res. 87, 2999–3019.

Jakosky, B.M., Haberle, R.M., 1992. The seasonal behavior of water on Mars. In: Kieffer, H.H., Jakosky, B., Snyder, C., Matthews, M. (Eds.), Mars. Univ. of Arizona Press, Tucson, pp. 969–1016.

Jakosky, B.M., Henderson, B.G., Mellon, M.T., 1995. Chaotic obliquity and the nature of the martian climate. J. Geophys. Res. 100, 1579–1584.

Laskar, J., Levrard, B., Mustard, J.F., 2002. Orbital forcing of the martian polar layered deposits. Nature 419, 375–377.

Laskar, J., Correia, A.C.M., Gastineau, M., Joutel, F., Levrard, B., Robutel, P., 2004. Long term evolution and chaotic diffusion of the insolation quantities of Mars. Icarus 170, 343–364.

Melosh, H.J., Raefsky, A., 1980. The dynamical origin of subduction zone topography. Geophys. J. Roy. Astron. Soc. 60, 334–354.

Milkovich, S.M., Head III, J.W., 2004. Characterization and comparison of layered deposit sequences around the north polar cap of Mars: identification of a fundamental climatic signal. Lunar Planet. Sci. XXXV. Abstract 1342.

Murray, B.C., Soderblom, L.A., Cutts, J.A., Sharp, R.P., Milton, D.J., Leighton, R.B., 1972. Geological framework of the south polar region of Mars. Icarus 17, 328–345.

Nomanbhoy, M., Murray, B., Pathare, A., Koutnik, M., Byrne, S., 2004. Morphological evidence for the large-scale evolution of martian north polar troughs? Lunar Planet. Sci. XXXV. Abstract 1694.

Nye, J.F., 1952. A comparison between the theoretical and the measured long profile of the Unteraar glacier. J. Glaciol. 2, 103–107.

Nye, J.F., 2000. A flow model for the polar caps of Mars. J. Glaciol. 46, 438–444.

Nye, J.F., Durham, W.B., Schenk, P., Moore, J., 2000. The instability of a south polar cap on Mars composed of carbon dioxide. Icarus 144, 449–455.

Paige, D.A., Ingersoll, A.P., 1985. Annual heat balance of martian polar caps: Viking observations. Science 228, 1160–1168.

Paige, D.A., Bachman, J.E., Keegan, K.D., 1994. Thermal and albedo mapping of the polar regions of Mars using Viking thermal mapper observations. 1. North polar region. J. Geophys. Res. 99, 25959–25991.

Paterson, W.S.B., 1994. The Physics of Glaciers, third ed. Pergamon Press, Oxford.

Pathare, A.V., Paige, D.A., Turtle, E., 2005. Viscous relaxation of craters within the martian South Polar Layered Deposits. Icarus 174, 396–418.

Richardson, M.I., 1999. The martian water cycle. In: Fifth Int'l Conf. on Mars. Abstract 6021.

Roark, J.H., Frey, H.V., 2001. GRIDVIEW: recent improvements in research and education software for exploring Mars topography. Lunar Planet. Sci. XXXII. Abstract 1618.

Smith, D., 18 colleagues, 1999. The global topography of Mars and implications for surface evolution. Science 284, 1495–1503.

Smith, M.D., Pearl, J.C., Conrath, B.J., Christensen, P.R., 2001. Thermal Emission Spectrometer results: Mars atmospheric thermal structure and aerosol distribution. J. Geophys. Res. 106 (E10), 23929–23945.

Squyres, S.W., 1979. The evolution of dust deposits in the martian north polar region. Icarus 40, 244–261.

Thomas, P.C., Squyres, S., Herkenhoff, K., Howard, A., Murray, B., 1992. Polar deposits of Mars. In: Kieffer, H.H., Jakosky, B., Snyder, C., Matthews, M. (Eds.), Mars. Univ. of Arizona Press, Tucson, pp. 767–795.

Tomasko, M.G., Doose, L.R., Lemmon, M., Smith, P.H., Wegryn, E., 1999. Properties of dust in the martian atmosphere from the Imager on Mars Pathfinder. J. Geophys. Res. 104 (E4), 8987–9008.

Toon, O.B., Pollack, J.B., Ward, W., Burns, J.A., Bilski, K., 1980. The astronomical theory of climatic change on Mars. Icarus 44, 552–607.

Touma, J., Wisdom, J., 1993. The chaotic obliquity of Mars. Science 259, 1294–1297.

Ward, W.R., 1992. Long-term orbital and spin dynamics of Mars. In: Kieffer, H.H., Jakosky, B., Snyder, C., Matthews, M. (Eds.), Mars. Univ. of Arizona Press, Tucson, pp. 767–795.

Ward, W.R., Rudy, D.J., 1991. Resonant obliquity of Mars? Icarus 94, 160–164.

Zuber, M., 20 colleagues, 1998. Observations of the north polar region of Mars from the Mars Orbiter Laser Altimeter. Science 282, 2053–2060.

Zwally, H.J., Fountain, A., Kargel, J., Kouvaris, L., Lewis, K., MacAyeal, D., Pfeffer, T., Saba, J.L., 2000. Morphology of Mars north polar ice cap. In: 2nd International Conference on Mars Polar Science and Exploration. LPI Contrib. 1057, pp. 192–193.